Finite-Difference Time-Domain Simulations of Light Scattering from Retinal Photoreceptors

by

Samer S. Abdallah

A thesis
presented to the University of Waterloo
in fulfillment of the
thesis requirement for the degree of
Master of Applied Science
in
Electrical and Computer Engineering

Waterloo, Ontario, Canada, 2007

I hereby declare that I am the sole author of this thesis. This is a true copy of the thesis, including any required final revisions, as accepted by my examiners.

I understand that my thesis may be made electronically available to the public.

Abstract

Recently, a novel optical imaging technique was successfully used in measuring the functional response of living retinal tissues. The technique, functional ultra high resolution optical coherence tomography, measures localized differential changes in the retina reflectivity over time resulting from external white light stimulation. This result can be used to develop a non-invasive diagnostic method for the early detection of retinal diseases. However, the physiological causes of the experimentally observed optical signals, most of which originate from the photoreceptors layer, are still not well understood. Due to the complexity of the photoreceptors, using purely experimental methods to isolate the changes in light reflectivity corresponding to individual physiological processes is not feasible. Therefore, we have employed the finite-difference time-domain method to model the changes in light scattering patterns of the photoreceptor cells caused by light-induced physiological processes. Processes such as cell swelling, cell elongation and hyperpolarization of double-lipid membrane structures were simulated by changing the size parameters and optical properties of the cells components. Simulation results show that the hyperpolarization of double-lipid membranous structures and cell swelling are the most likely causes for the experimentally observed changes in optical reflectivity. A number of experiments were suggested to verify the conclusions drawn from this numerical work. This numerical work includes an analysis of various errors in FDTD computational models.

Acknowledgements

I am deeply grateful to my thesis advisors Prof. Omar Ramahi and Prof. Kostadinka Bhizeva for their guidance and for their encouragement and care of me during the past three terms of my MASc studies. Also, I would like to acknowledge the invaluable help of Alex Iolov who contributed significantly to the numerical dispersion work.

I am extremely grateful for the patience, time and efforts the two readers of my thesis, Prof. Magdy Salam and Prof. Dayan Ban, have spent in reviewing this work.

My sincere thanks go to my friends Ahmad Shamy, Ahmad El-Sayed, Sami Khashan, Omar Halabieh, Zeid Abou Shahine and many others who believed and still believe in me.

I am deeply and forever indebted to my parents for their love, support and encouragement throughout my entire life.

To Lebanon, my childish, special and crazy country

To Mirva, the source of my Qi

Contents

List of Tables

List of Figures

Chapter 1

Introduction

1.1 Overview

Retinal diseases such as Diabetic Retinopathy, Age related Macular Degeneration (AMD) and Retinitis pigmentosa are characterized by the progressive loss of the visual perception. Currently, electroretinography (ERG) is the only clinically approved method for probing the functional response of the retina. However, ERG lacks spatial and depth resolution, and can only provide an integrated electrical response from all layers of the retina. Therefore, various optical imaging techniques were developed for the diagnosis of retinal diseases. Most of these techniques rely directly or indirectly on light scattering in tissue especially for the wavelength range 600-1100nm [1]. By providing in-vivo 3D high-resolution images of the retinal morphology at the cellular level, these techniques can detect the abnormal development of biological tissue caused by retinal pathologies.

Previous studies have demonstrated that, in addition to providing in-vivo 3D high resolution morphological images of the retina, optical coherence tomography (OCT) can be used to probe the functional response of living photoreceptor cells resulting from external

light stimulation [2, 3, 4]. The technique, called functional ultra high resolution OCT (fUHROCT) measures localized differential changes in the retinal reflectivity over time resulting from light stimulation of the retina. Using fUHROCT, it was shown that a significant temporal change in optical reflectivity occurs in the photoreceptor cells after the external light stimulation of the living retinal tissue.

Since OCT is sensitive to changes in the magnitude and spatial distribution of the index of refraction, to the shape and surface quality and to the absorption properties of the cell tissues, the detected functional response indicates the presence of physiological processes that affect the structural and optical properties of the photoreceptor cells when stimulated by external light. Therefore, retinal diseases which alter these photo-active physiological processes can be diagnosed by detecting changes in the functional response. This potential diagnostic method based on fUHROCT will be able to detect the functional abnormalities of the photoreceptor cells at a very early stage of retinal diseases before they develop into permanent physiological and morphological changes (such as the gradual death of the photoreceptor cells and their detachment from the retinal tissue).

Currently, the cellular mechanisms behind the experimentally observed changes in reflectivity are not well understood. This is a very challenging task using pure experimental methods given the complex nature of the photoreceptor cells. Various physiological processes such as the hyperpolarization of the cell membranes and the propagation of the action potentials can affect the signal detected by the fUHROCT system by changing the index of refraction of biological tissue [5, 4, 6]. Many of these processes occur simultaneously (within the fUHROCT time resolution) and are localized in a very small volume in biological tissue comparable to the pixel size of fUHROCT. Therefore, isolating individual physiological processes as the cause of particular optical changes is not trivial and in most cases not feasible experimentally.

Computational electromagnetics can be employed in investigating the origins of the functional response. Various techniques ranging from integral equations solvers to differential equations solvers can be used to model light scattering from photoreceptor cells. Among these techniques, the finite-difference time-domain method (FDTD) stands out for the simplicity it allows in modeling complex structures such as the photoreceptor cells. In the recent year, the FDTD method has been successfully employed in studying the effect of diseases such as cancer on light scattering simulations from biological cells [7, 8, 9, 10].

This work presents computational models of the photoreceptor cells based on the FDTD method. A processing scheme for light scattering computations was developed, validated and successfully applied in simulating the functional response of the photoreceptor cells. In addition, numerical errors in the results were quantified. Based on the simulation results, a theory was conceived to provide an explanation of the experimental results of the study on the functional response of the retina [2]. The work is concluded by suggesting an experiment to test the provided explanation.

1.2 Thesis Outline

Chapter 2 presents background information about fUHROCT and the photoreceptor cells. In Chapter 3, the FDTD method and its application to light scattering simulations are discussed. In addition, a general model of the photoreceptor cells is proposed in combination with several hypotheses about the origins of the functional response. Simulation results are presented and analyzed in Chapter 4. Analysis of numerical errors in FDTD light scattering simulations is given in Chapter 5. Finally, Chapter 6 concludes the study and outlines the future work.

Chapter 2

Background

2.1 Optical Coherence Tomography

Optical coherence tomography (OCT) is an optical imaging technique offering sub-micrometer resolution in axial and lateral directions. It has been widely adopted in the non-invasive *in-vivo* imaging of biological tissues and in particular the retinal tissue [11]. OCT is based on low coherence interferometry as demonstrated in fig. 2.1. A beam-splitter divides the source light beam and directs it toward two reflective mirrors. A photo-detector measures the magnitude of the central interference fringe of the back reflected optical beams. As the measurement mirror changes position, a coherent light source will show a constant amplitude interferogram. However, when a partially coherent light source is used, interference occurs only when the difference in the optical paths of the two beams is smaller than the coherence length of the light source, and as a result the interferogram shows a Gaussian-like modulation in the amplitude. In an OCT system, the magnitude of the interference signal is proportional to the power of back-reflected light, while the time delay determines the position within the imaged object from which the back-reflected light originated. The

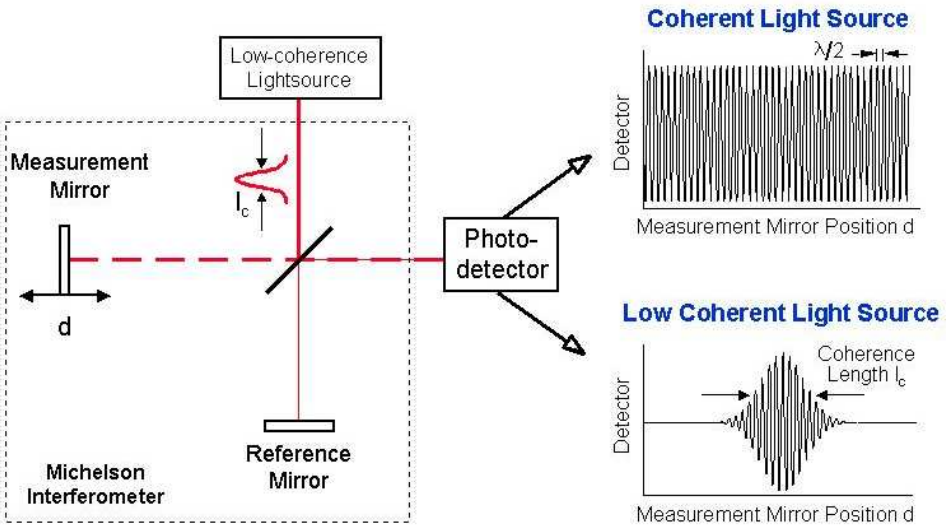

Figure 2.1: Principle of optical coherence tomography: a low coherent light source in a Michelson interferometer ([12]).

ability of an OCT system to image biological tissues depends on the optical reflectiveness of the tissue. In addition, the differences in the power of light reflected from various portions of the tissue provide the contrast in the image. The optical properties of biological tissues are described by their index of refraction n, the roughness of their surface and the degree of their homogeneity. The refractive index is a fundamental physical property given by the square root of the product of the relative permittivity ϵ_r with the relative permeability μ_r (i.e. $n = \sqrt{\epsilon_r \mu_r}$). In general, the refractive index is a complex number $n_c = n - i\kappa$ where n measures how much the speed of light v_{ph} is reduced inside the medium as compared to its speed in vacuum c ($n = \frac{c}{v_{ph}}$) and κ is the coefficient of absorption of light in the medium. The index of refraction is the main parameter in the Fresnels equations which describe the behavior of light (reflection and transmission) when propagating from a half-space medium to another with different index of refraction. For the case of normal incidence, the reflectivity coefficient R, given in eq.2.1, shows that the amount of light reflected at the interface

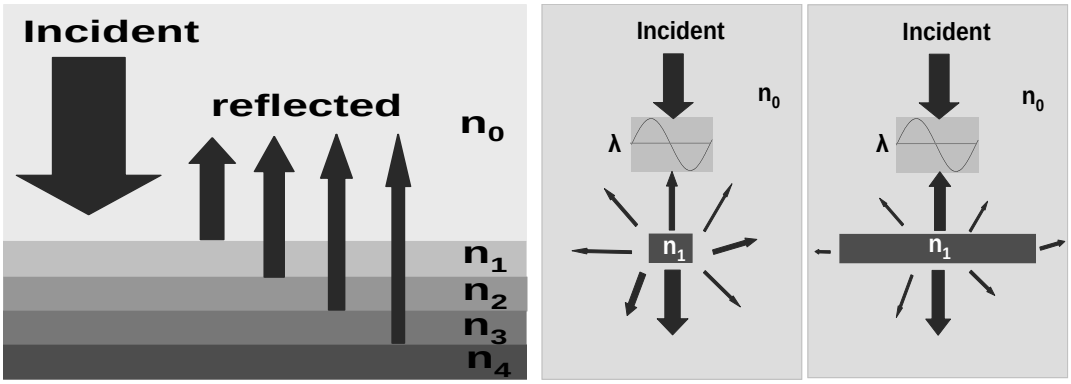

Figure 2.2: Physical parameters affecting the amount of back-reflected light: a) change in the index of refraction, b) change in the physical size.

separating the two mediums is proportional to the square of the difference of the refractive indexes. Therefore, a light beam incident on an object consisting of a stack of layers (fig. 2.2(a)), each with a different refractive index, will back-reflect at each of the interfaces and consequently, the OCT cross-sectinal image of the object will show the various layers with the contrast corresponding to the amount of back-reflected light.

$$R = \frac{E_{reflected}}{E_{incident}} = \left(\frac{n_1 - n_2}{n_1 + n_2}\right)^2 \tag{2.1}$$

In addition to the index of refraction, the physical size of the scattering object as compared to the wavelength affects significantly the amount of back-reflected light (fig. 2.2(b)). In general, the amount of back-reflected light increases when the size of the scattering object increases (fig. 2.2(b)).

2.2 Retinal Photoreceptors

The retina is a thin ($\sim 500\mu m$) transparent and multi-layered tissue that lines the back of the eye. In vertebrate retinal tissues, The photoreceptor layer constitutes the back layer (taking the direction of incident light as reference). Photoreceptors cells are sensory

neurons that detect visible light photons (wavelength ranging from $380nm$ to $780nm$) and generate the electrical neural signal. All vertebrates retina contain two types of photoreceptors, rods and cones which are similar in their basic structure. In addition, vertebrate rods and cone photoreceptor cells show a very uniform organization with some variations in size and shape. These variations depend on the type of species and the location within the retina relative to the fovea. In general, a single photoreceptor (cone or rod) can be divided into three major parts:

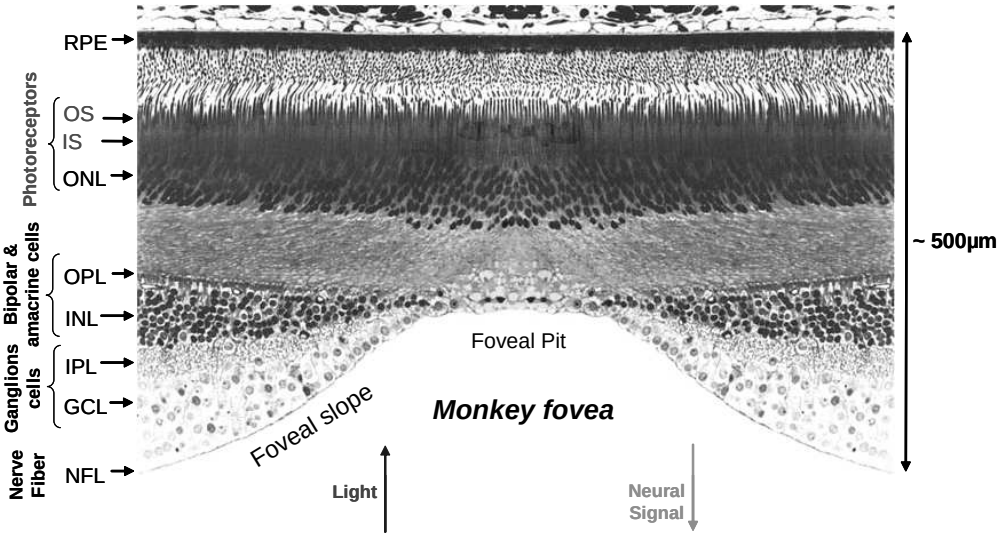

Figure 2.3: A cross-sectional image of the foveal region in a monkey's retinal tissue: RPE-Retinal Pigment Epithelium layer, OS-Outer Segment, IS-Inner Segment, ONL-Outer Nuclear Layer, OPL-Outer Plexiform Layer, INL-Inner Nuclear Layer, IPL-Inner Plexiform Layer, GCL-Ganglion Cell Layer, NFL-Nerve Fiber Layer. ([13])

1. Head, almost entirely occupied by the nucleus. The nucleus is surrounded by a small volume of cytoplasm. The head forms the outer nuclei layer of the retina.

2. Neck, known as the inner segment (IS) of the photoreceptor. The IS provides the metabolic support for the cell.

3. Tail, known as the outer segment (OS) of the photoreceptor. The OS contains the visual pigments responsible for the detection of light.

Fig. 2.3 shows a cross-sectional image of the foveal region in a monkey's retinal tissue. The figure shows the locations of the retinal pigment epithelium layer (RPE) and the photoreceptors layer. Fig. 2.4 presents a schematic of rod and cone photoreceptors. The schematic shows the basic organization of the cells (Nucleus, IS, OS), their main components (mitochondria, microtubules, discs, ...), and highlights the basic structural differences between the rod and cone photoreceptors (tapered cone OS and IS vs. cylindrical rod IS and OS ...). The rest of this section discusses various structural and functional characteristics of the photoreceptor cells that are relevant in constructing the models of the photoreceptor cells and in understanding the physiological processes causing the experimentally observed optical signals.

2.2.1 Inner Segment

The IS can be divided into two parts, the myoid and the ellipsoid. The ellipsoid, to the side of the OS, is densely packed with mitochondria which provide the energy needed for the proper functioning of the cell. In mammals and most vertebrates, the ellipsoid mitochondria are typically long, slender (filamentous mitochondria) and are packed parallel to the axis of the IS and along the full length of the ellipsoid[15]. Furthermore, the mitochondria comprise 74-85% of the volume of cone ellipsoids and 54-66% of the volume of rod ellipsoids in macaque [16]. Fig. 2.5 shows how the ellipsoid of a cone photoreceptor is packed with mitochondria. The physical dimensions of the ellipsoids change as a function of the distance from the fovea. Rod ellipsoids in the central regions are thin, long, and cylindrical whereas, at increasing eccentricities, the rod ellipsoids become larger in diameter and shorter in length [16].

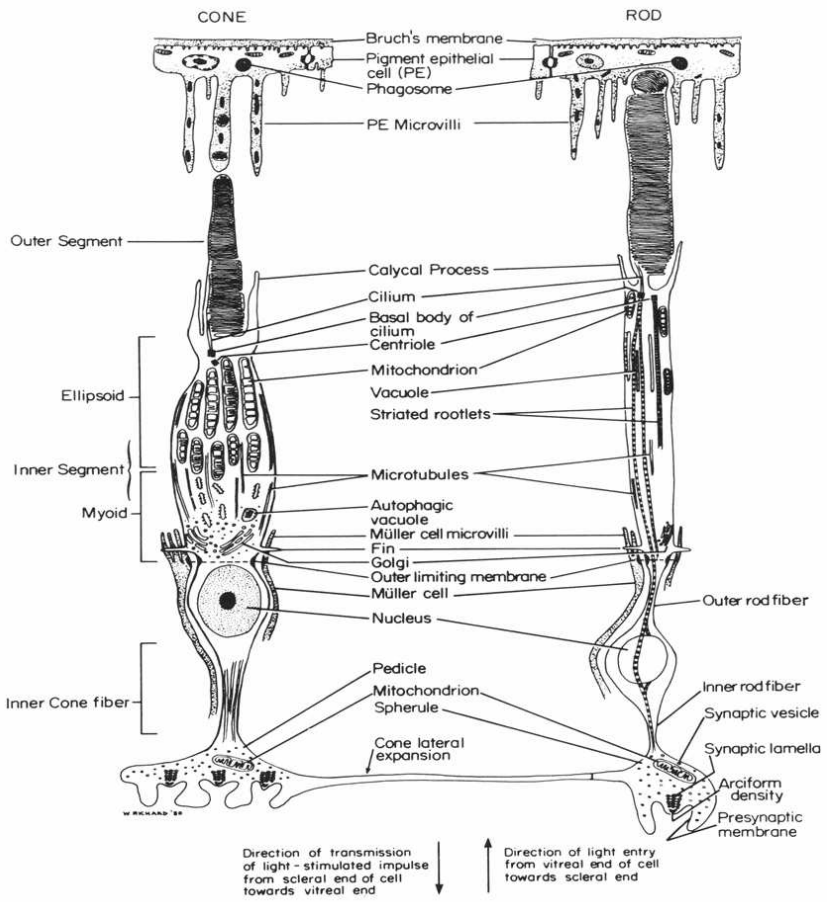

Figure 2.4: A schematic of rod and cone photoreceptors showing their basic organization and their main components ([14]).

The myoid, to the side of the nucleus, contains a complex system of tubules, vesicles and vacuoles that consists of the rough and smooth endoplasmic reticulum, the golgi apparatus, secretory vesicles, and a multiplicity of transport vesicles that interconnect these various organelles. Also, longitudinal filaments are abundant, running the full length of the IS and are grouped in bundles around the periphery of the cell, parallel to the long axis. In general, filaments (microtubules, neurofilaments and actin microfilaments) account for about 25% of the protein mass of neuron cells. They form the cytoskeleton which is the

major determinant of the shape of the cell. On the functional level, the myoid provides the proteins involved in the synthesis of the visual pigments (rhodopsin molecules) of the outer segments. In addition, the myoid provides the structural mechanisms that allow for photo-induced mechanical movements in the photoreceptors [14]. The photo-induced movements consist of either the contraction or the expansion (depending on the lighting conditions) and/or the alignment of the cells towards the pupillary center. These movements are carried out through alteration of lengths of the filaments of the IS (in particular in the myoid part) and maybe through the involvement of various micro-organelles such as the microtubules, fins and the calcycal processes.

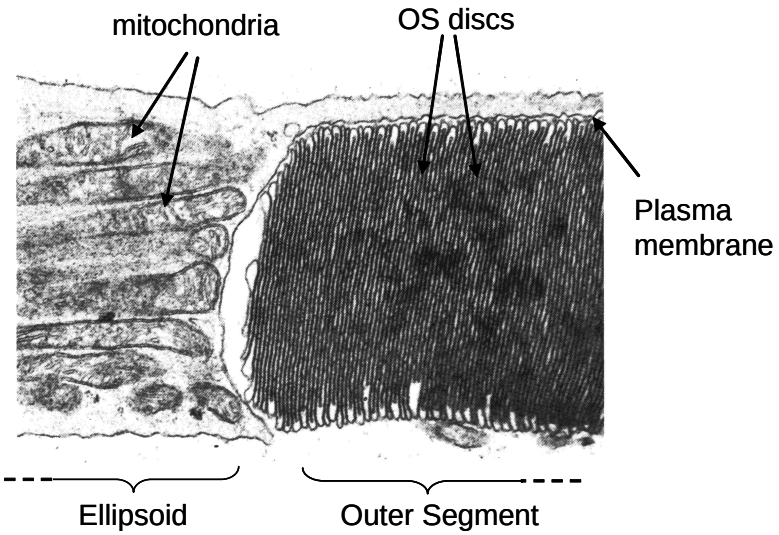

Figure 2.5: A cross-sectional image showing the end of the ellipsoid and the beginning of the OS in a cone photoreceptor ([17])

2.2.2 Outer Segment

The OS is comprised of thousands of densely packed double-lipid membrane discs stacked on top of each other like a roll of pennies in a bank wrapper (fig. 2.5. Each disc is

pocked with complex molecules called rhodopsin which consists of a small light-absorbing molecule attached to a large membrane-spanning protein. This periodic structure increases the surface area of the membrane allowing the OS of a single photoreceptor cell to contain a remarkably large number of these visual pigments ($\sim 10^8$) [18]. Moreover, this structure enhances light absorption properties because the dipole movement of the rhodopsin chromophore is transverse to the receptor axis [19]. On the functional level, the OS is the location of the transduction of the neural signal in the photoreceptors: The OS plasma membrane (outer membrane) provides the site where the action potential is generated.

On the structural level, the OS discs are continuously being generated as a series of uniform invaginations of the cell's plasma membrane, which leads to this regular structure. On average, there are 80-90 discs assembled daily (in human rod cells [20]) and it takes a few days for a disc (about 9-13 days in monkeys photoreceptors) to migrate the entire length of the OS before its disintegration by phagocytosis in the Retinal Pigment Epithelium layer (RPE). It has been shown that light stimulates the rate of discs addition in both rods and cones and that the shedding of discs is synchronized with the opening of the eye [21] such that the outer segment remains of constant length [22]. The highly ordered regularity of the disc arrangement and structure may be disrupted, more easily in cones than in rods, by a variety of traumas such as fixation artifact, visible light of too long duration or too high intensity, retinal detachment, vitamin A deficiency, thermal trauma and a result of non-Q-switched laser irradiation, low-energy-level laser damage, aging and osmotic shock [14].

One of the most consistent differences between rods and cones are found in their outer segment discs. In cones, the discs are continuous with the plasma membrane, while in rods, the newly created discs become independent intracellular organelles by pinching off from the plasma membrane [23, 24]. Therefore, most cone discs retain the continuity with

the plasma membrane, and hence, are open to the extracellular space whereas rod discs form closed saccules, isolated from the extracellular space [14]. Consequently, the rod discs show osmotic expansion and shrinkage [25]. In addition, rod discs have their double-lipid membranes further apart near the edges than at the center. The rod disc edge stains more heavily than the rest of the saccule and it has greater resistance to deformation. It has been suggested that a calcium-binding protein may be located at the disc edge close to the plasma membrane. Calcium has been implicated in the transmitter process, being released when light acts on the rhodopsin molecule[26].

2.2.3 Rod Photoreceptor

Rod photoreceptors, named for their cylindrical shape, are used for night and peripheral vision. They are sensitive enough to detect a single photon however their response time is slow and consequently they cannot detect image changes faster than $100ms$ [18]. Some vertebrates (e.g. rabbits) have only rod photoreceptors in their retina.

2.2.4 Cone Photoreceptor

Cone photoreceptors are named as such due to the conic shape of their IS. The IS and OS of a cone photoreceptor are independently tapered structures and the entire cell forms a clearly tapered structure [27]. Cone photoreceptors contains three types of photosensitive pigment (rhodopsin) which are responsible for detecting colors. Moreover, a cone cell can detect faster changes in the perceived images but it requires 100 times more photons than a rod cell to get activated. In human retina, cone photoreceptors are concentrated in the fovea part and therefore they are sensitive to direct light whereas rod photoreceptors are more sensitive to scattered light. [18]

2.2.5 Mechanism of Signal Transduction

Ion Channels

In neural cells, the action potential is created by a change in the ionic fluxes across the plasma membrane. Cytoplasmic membranes are made of double layers of phospholipids. Phospholipid molecules have hydrophilic heads and hydrophobic tails. The hydrophobic tails join to the inside of the membrane to prevent the crossing of water and ions while the polar hydrophilic heads face the aqueous medium. However, membrane spanning proteins called ion channels form active gateways for the ions to cross the membrane. Ion channels have three properties: conducting ions, recognizing and selecting specific ions, and opening and closing in response to specific electrical, mechanical, or chemical signals. Also, even though ion channels are highly selective, they conduct large flows of ions, up to 100 million ions/channel/sec [18]. In addition, the switching time in ion channels is less than $10\mu sec$ allowing the membrane potential to change quickly, up to 500 V/sec.

Photo-activation

The photo-activation of the visual pigments in the OS of rods and cones triggers a three-stage cascade of biochemical processes which leads to a change in the ionic fluexes across the plasma membrane, and consequently a change in the membrane potential. A key molecule in the chain is the nucleotide cyclic guanosine monophosphate (cGMP) [18]. In the dark, the concentration of cGMP molecules is relatively high and consequently, the cGMP-gated channels are in an open state and allowing the inward current they carry to maintain the cell in a relatively depolarized state. When light activates the visual pigment, a conformal change occurs in the molecular configuration of the rhodopsin. The photoactivated rhodopsin stimulates an enzyme which reduces the concentration of cGMP in the cytoplasm. This reduction in cGMP concentration closes the cGMP-gated channels

and stop one of the dark currents, thus creating an imbalance in the "dark" current flowing between the inside and the outside medium and consequently causes the hyperpolarization of the photoreceptor.

Dark Current

In dark conditions, two ionic currents dominate the photoreceptor. Inward current flows through cGMP-gated channels, which are confined to the OS, while an outward K+ current flows through none-gated K+ selective channels, which are confined to the IS. The outward current carried by the K+ channels tends to hyperpolarize the photoreceptor toward the equilibrium potential for K+ (around -70 mV). The inward current tends to depolarize the photoreceptor. The photoreceptor is able to maintain steady intracellular concentrations of Na+ and K+ because its IS has a high density of Na+ and K+ pumps, which pump out Na+ and pump in K+ [18].

2.2.6 Light Adaptation

In addition to the pupil of the eye, there exist other photomechanical mechanisms in the RPE layer and the myoid part of the IS and which regulate the amount of light striking the photoreceptor cells. The RPE layer contains lots of melanin granules. The pigment granules absorb the stray photons, preventing their reflection back into the photoreceptors, which would cause images to blur. They also protect the cells from too much exposure to light radiation. In the dark, the pigments move toward the RPE cell base and in light towards the Outer Limiting Membrane (OLM) so that the rods, which are more light-sensitive, are well surrounded by the pigment during bright light conditions and vice versa in the dark. Furthermore, depending on the light conditions, the myoid part of the IS of rods and cones alters its length. In the light, the rod myoids elongate and cone myoids contract, while in the dark, rod myoids contract and the cone myoids elongate. This

alteration of the lengths of the photoreceptor cells occur at the rate of 1-2μm/min [28]. In photomechanical movements, the myoid can elongate or shorten by up to 90% [28]. These photomechanical movements can affect light scattering by changing the dimensions of the photoreceptor cells in the case of myoid length alteration or through the effect of having a sheath of absorbing material around the OS in the case of light-induced pigment migration.

Experimental studies on suspensions of rod OS found that the photo-excitation of rhodopsin induced changes in the light-scattering profiles. It has been suggested that the causes behind these light-scattering signals lie in the modification of the size or the separation of the disks, the swelling of the rod OS [29] or its shrinkage [30, 31]. In the IS, the generation of the neural signal is accompanied by an increase in the metabolic activity. The activity of the photoreceptor when exposed to light or not causes some staining differences in the ellipsoid mitochondria [32] which might indicates a change in the chemical composition or the density, both of which can cause a change in the refractive index and consequently a change in its light scattering pattern.

2.3 Functional Response of the Retina using OCT

Fig. 2.6 shows the schematic of a fUHROCT system used in probing the functional response of the retinal tissue. A white light source provides the external stimulation of the retina while an infra-red beam scans the retina in the lateral directions. The position of the reference mirror specifies the scanning depth inside the retina. A spectrometer measures the reference and the back-reflected signals. A processing unit computes the interferogram and outputs a depth specific signal versus time.

Functional imaging of the retina was conducted on rabbit retina (rod photoreceptors) [2], rat retina [3] and frog retina (rod photoreceptors) [4] and all studies reported similar results. The external white light stimulation of a living retinal tissue caused a significant

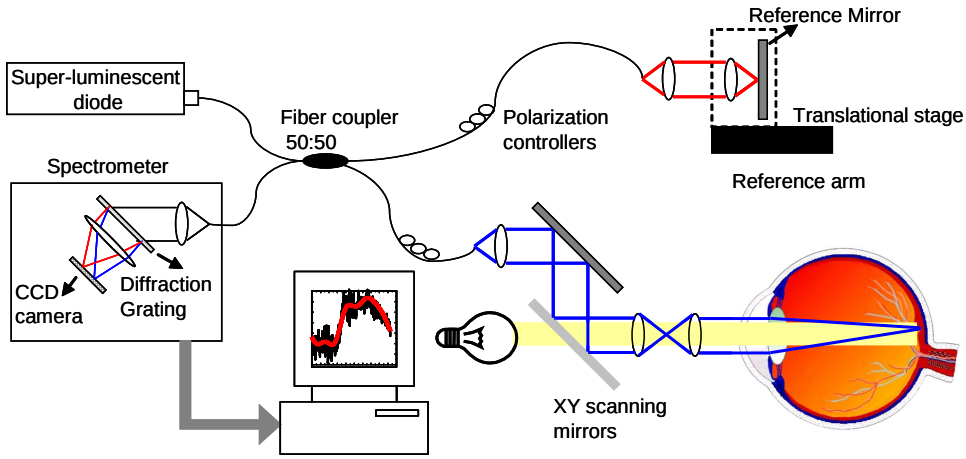

Figure 2.6: General schematic of a fUHROCT system used to probe the functional response of the retina (to our knowledge, there are no published data about fUHROCT applied on human retina yet) ([12]).

increase in optical reflectivity of the OS and a significant decrease in the optical reflectivity of the IS part. The change in optical reflectivity and the ERG signal (indicating the living state of the photoreceptors) are detected simultaneously after the short stimulation of the retinal tissue. The amount of change in the intensity of back-reflected light is proportional to the intensity of the stimulation [2]. The change in reflectivity lasts for couple seconds after the stimulation is applied. Currently, the origins of these optical signals are still unknown.

2.4 Optical Properties of Photoreceptors

Constructing electromagnetic models of the photoreceptor cells for light scattering computations requires knowing the optical properties and size parameters of the cells and their main components. However, many of these parameters have some dependencies on the type of species, the location of the photoreceptor within the eye, ... Moreover, the values

Cell Component	Index	Reference
External medium	1.35	[7]
Cytoplasm	$1.35 - 1.37$	[33]
	1.35	[34]
	1.365	[35]
Cell Membrane	$1.46 - 1.48$	[36]
	1.48	[1]
Nucleus	1.39	[7]
Rod Outer Segment	1.410	[37, 38]
Cone Outer Segment	> 1.41	[37]
	1.385	[14]
IS	1.353	[14]
Cone IS - myoid	1.36	[14]
Cone IS - ellipsoid	1.39	[14]
Rod IS - myoid	1.36	[14]
Rod IS - ellipsoid	1.40	[14]
Mitochondria	≈ 1.43	[14]

Table 2.1: Refractive index values of cell components taken from published data in the scientific literature.

of some parameters such as the dielectric properties of some cell components are only available for different type of cells and from various species. Furthermore, the majority of the values of indexes of refraction found in the scientific literature do not include the complex components that model the absorption effects and the frequency dependence. However, since the retina is a transparent tissue, it is assumed that the refractive index values obtained constitute a sufficient approximation for first order calculations. Table 2.1 presents the refractive index values of the main components of rods and cones. Since the refractive index of a material is proportional to the density of proteins and lipids, the cytoplasm and surrounding medium has smaller values compared to the nucleus and the mitochondria. The double-lipid membrane has the highest refractive index due to the polarity of its molecules. The refractive index of the OS is higher than that of the IS, since it includes the contribution of the discs which are made of the double-lipid membrane. The size parame-

Cell Component	Parameter	Value	Reference
Mitochondria	diameter	$> 0.2\mu m$	[39]
		$0.4 - 0.5\mu m$	[1]
		$0.1 - 0.5\mu m$	[34]
	length	up to $10\mu m$	[34]
Microtubules	diameter	$25 - 28nm$	[18]
	length	up to 0.1 mm	[18]
Vacuoles	diameter	$20 - 80nm$	[40]
Rod OS	diameter	$\approx 1\mu m$	[37]
	length	$\simeq 10\mu m$	[37]
Cone OS	diameter	$0.9\mu m$	[14]
Cone IS	Diameter	$2.5 - 3\mu m$	[37]
		$1.5 - 2.1\mu m$	[14]
Plasma membrane	thickness	$6 - 8nm$	[18]

Table 2.2: Typical sizes of segments and organelles in photoreceptor cells of various species taken from published data in the scientific literature.

ters are presented in table 2.2. Since the size parameters of a photoreceptor cell as whole are comparable to the wavelengths of the spectrum of the imaging beam, it is expected that changes in these parameters will cause a significant change in the light scattering pattern. The cylindrical shape of photoreceptor cells, their dimensions and the fact that their refractive index is higher than the surrounding medium are the reasons behind their waveguiding properties [14]. Among the waveguide properties of photoreceptors is that the light at the shorter wavelengths of the visual spectrum couples better to the inside of the photoreceptor cell than the light at the longer wavelengths. So far, various analytical and semi-analytical models were used to represent the photoreceptors as dielectric waveguides and to explain some of the experimentally observed effects such as the Stiles-Crawford effect which describes the directional sensitivity of the cone photoreceptors [41]. In another approach, the photoreceptor was modeled as a light collector given its tapered structure at the IS-OS interface and the fact that the refractive index of the OS is greater than that of the IS. In summary, the structure of the photoreceptor plays a significant role in light

detection.

2.5 Conclusions

This chapter discusses OCT and its applications in the functional imaging of the living retina. Also, the chapter presents a summarized description of the photoreceptors which is necessary for a basic understanding of these complex cells. Various functional, structural and optical properties of the photoreceptor cells were presented. The discussion was very helpful in guiding the modeling work and in providing the theoretical basis for explaining the origins of the experimentally observed signals.

Chapter 3

General Photoreceptor FDTD Model

3.1 Introduction

In 1966, Yee introduced the FDTD method for solving Maxwell's equations [42]. Because of its simplicity in modeling complex structures, the FDTD method has been used to study the electromagnetic interaction with organic materials [8]. In Yee's algorithm, Maxwell's curl equations are solved by implementing time and space derivatives of the electric and magnetic fields using second order accurate central finite-difference expressions. Space is discretized according to a special Cartesian grid, Yee's lattice, which indirectly implements Maxwell's divergence equations. At each time instant, the electric and magnetic fields components of each grid cell are computed using the stored values of the previous time instant and the values of fields in the neighboring cells. Eq. 3.1 demonstrates the FDTD algorithm for computing the x-axis component of the magnetic field at grid cell (i,i,k) at time instant n where ρ and $\rho^{'}$ are respectively the electric and magnetic resistivity

(equations for the other fields components are similar).

$$
\begin{aligned}
H_x\big|_{i,j,k}^{n+1/2} = & \left(\frac{1-\frac{\rho'_{i,j,k}\Delta t}{2\mu_{i,j,k}}}{1+\frac{\rho'_{i,j,k}\Delta t}{2\mu_{i,j,k}}}\right) H_x\big|_{i,j,k}^{n-1/2} \\
& + \left(\frac{\frac{\Delta t}{\mu_{i,j,k}}}{1+\frac{\rho'_{i,j,k}\Delta t}{2\mu_{i,j,k}}}\right)\left(\frac{E_y\big|_{i,j,k+1/2}^{n} - E_y\big|_{i,j,k-1/2}^{n}}{\Delta z} - \frac{E_z\big|_{i,j+1/2,k}^{n} - E_z\big|_{i,j-1/2,k}^{n}}{\Delta y}\right)
\end{aligned}
\tag{3.1}
$$

The solutions are obtained in the time domain and therefore, only one simulation run is needed to obtain results over a wide spectrum [10]. To ensure stability of the solution, the time step is chosen such that the Courant factor $C = \frac{v\Delta t}{\Delta x} < \frac{1}{\sqrt{dim}}$ everywhere in the computational domain (dim is the number of dimensions). Although FDTD simplifies the modeling process, it is computationally intensive in terms of memory, data storage, and processing requirements. In fact, for a Cartesian grid, if the resolution in n dimensions is doubled, the memory and storage needed increase by a factor of 2^n and the simulation duration increases by a factor $2^n \times C$. Moreover, solutions using the FDTD method suffer from numerical phase errors termed in the literature as "numerical dispersion" since the error depends on the wavelength. In second order FDTD, the numerical dispersion is proportional to the ratio of the mesh size to the wavelength $\frac{\Delta x}{\lambda}$ and consequently, the numerical dispersion can only be reduced by increasing the meshing resolution which consumes vast computing resources.

3.2 Methods

Fig. 3.1 shows the setup of FDTD simulations for light scattering from photoreceptors. The computational domain is divided into two regions. The inner region is the Total Field (TF) region where the total electromagnetic fields (total field = incident + scattered fields) are solved. The outer region is the Scattered Field (SF) region where only the

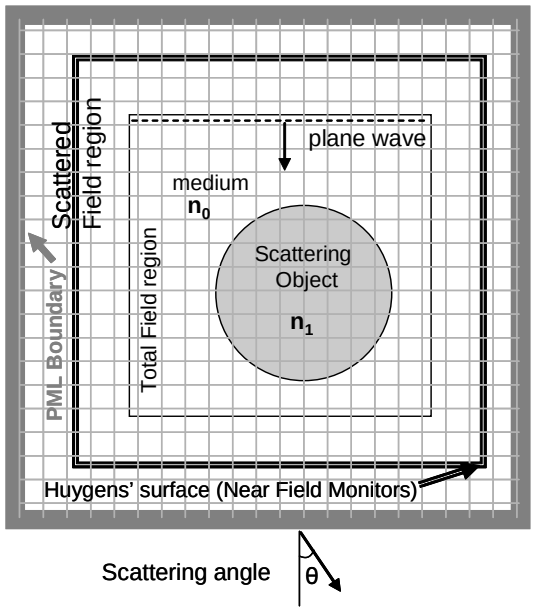

Figure 3.1: Typical setup of an FDTD simulation for light scattering computations.

scattered fields are solved. The incident wave is generated by forcing boundary conditions at the interface between the TF and the SF regions. The spectrum of the plane wave excitation spans $100nm$ around a central wavelength of $1040nm$ in order to match the properties of the fUHROCT system. The grid mesh size in each direction is chosen to resolve the smallest object of interest and to minimize the staircase of modeled circular shapes. Compared to the spectrum of interest, the grid size Δx_i was kept $\leq \frac{\lambda_{min}}{50}$, a value five times less than the maximum mesh size of $\frac{\lambda_{min}}{10}$ [43]. The field monitors are positioned in the SF region. To minimize storage and processing requirements, these monitors perform online Discrete Fourier Transform (DFT) on the near fields at the end of each time step. Once the simulation finishes, a post-simulation processing step performs an exact near-to-far field transform to obtain light scattering power at the far zone. Details about the FDTD algorithms and the near-to-far field transform can be found in Taflove's book on Computational Electromagnetics [43].

3.3 Validation

The approach outlined in the previous section was checked against analytical scattering solutions by Mie. Mie solutions are available for light scattering from an infinite cylinder or from a sphere. Fig. 3.2 compares the FDTD solution to Mie solution for light scattering from an infinite cylinder. The wavelength of the incident plane wave is set to $1\mu m$. The radius of the infinite cylinder is set to $1\mu m$ and its refractive index to 1.04. The FDTD results are in good agreement with Mie solutions however it shows a minimal discrepancy only for scattering angles larger than 160°. Similar discrepancies have been observed in the past and it has been proven that is it related to the grid size and the boundary conditions. This deviation can be attributed to the staircase effect when modeling circular shapes using Cartesian grids. The field monitors are put as close as possible (the monitors average results over 4 cells) to the TF-SF boundary. In theory, the distance of the TF-SF boundary to the scattering object should be as small as possible to minimize the numerical dispersion; however, it was found from several simulations and comparison with Mie solutions that the optimal distance of the TF-SF boundary to the object is close to $\frac{\lambda_{central}}{10} \times \frac{d_\lambda}{2}$ where d_λ is the extent of the object in the lateral directions in $\lambda_{central}$ units. Also, it was found that the distance of the PML (i.e. the boundaries of the computational domain) to the TF-SF boundary should be set close to $\frac{\lambda_{central}}{4}$.

3.4 Photoreceptor Model

3.4.1 Overview

In general, the photoreceptor cells can be modeled as long cylindrical structures with the axial direction aligned towards the center of the pupillary aperture [14]. The photoreceptors tend to incline to the best angular position for capturing light photons, i.e. orthogonal to

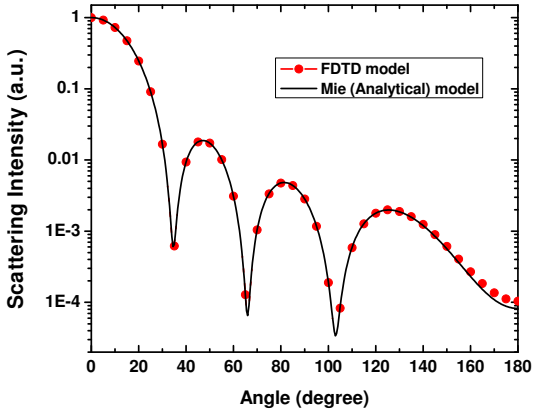

Figure 3.2: Validation of the FDTD method. Comparison of FDTD results with Mie theory predictions at $\lambda = 1\mu m$ for an infinite dielectric cylinder of radius $1\mu m$ and refractive index $n = 1.04$.

the pseudo-spherical wave front coming from the pupil [44, 45]. This simplifies the modeling of light scattering from a single photoreceptor cell since we only need to consider plane wave excitation with its wave vector parallel to the axial direction of the photoreceptor model. The darker color of the inner surface of the eye ball is due to the RPE layer since the whole retina is a thin ($\sim 500\mu m$), transparent and multilayered tissue, the photoreceptor layer being the bottom one. Therefore, in constructing the FDTD model of the photoreceptors, the various constituents of the cell are assumed to have a real index of refraction i.e. with no imaginary part modeling an absorption effect.

3.4.2 Objectives

Only nature is able to simulate itself.

The main objective of this work is to determine the physiological processes that are most likely responsible for the functional response of the photoreceptors. This response consists of the increase in light reflectivity of the OS and the decrease in light reflectivity of the IS. Therefore, we are primarily interested in the qualitative aspect of change in light scat-

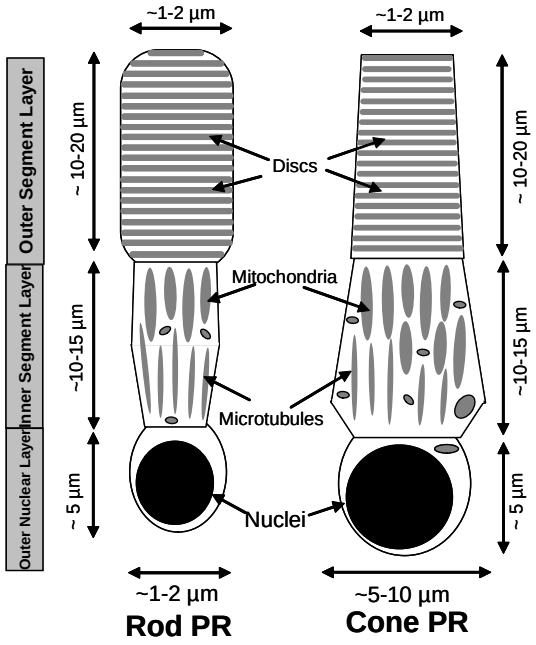

Figure 3.3: General FDTD model for cone and rod photoreceptor cells. The basic structure and organization of the cells is presented with a range of values for the size parameters.

tering as a function of the physiological processes, potential candidates for explaining the functional response. The candidate processes were selected based on the background study presented in chapter 2. The general model of the photoreceptor cells, shown in fig. 3.3, was constructed to allow the representation and easy testing of these processes on light scattering. In the following section, we present the candidate processes and the mechanisms by which they affect the light scattering patterns.

3.4.3 Hypotheses

External light stimulation of living photoreceptors causes a temporary increase in OS optical reflectivity and a decrease in IS's one. Both signals are recorded over time as a change in the power of backscattered light. Also, it has been shown [2] that the intensity

of optical response is proportional to the intensity of stimulus before saturation level is reached and that the response to some extent coincides with the electroretinogram (ERG) signal (differences exist in the rise time, the slope and the sign of change) indicating that the photoreceptor cells are living and generating the neural signal. Currently, the origins of the optical response are not known and since it is very difficult to determine the involved physiological processes using pure experimental techniques, we can only postulate potential processes and investigate numerically their effect on photoreceptors optical reflectivity. The following present some of these processes:

Membrane Hyperpolarization

It has been shown in [5] that changes in the membrane potential of neuron cells is associated with changes in its light scattering pattern. During the photo-transduction process, an action potential is generated in the OS which propagates through the IS to the synaptic terminals of the photoreceptors. The change of the membrane potential from -40mV to -70mV will enhance the alignment of the dielectric dipoles in the double-lipid membrane, therefore, increasing the refractive index of the membrane. This increase in the refractive index might cause an increase in reflectivity at the backscattered angles. From previous work [5], this increase in the refractive index can be assumed not to exceed the 5%.

Discs Hyperpolarization

In dark conditions, steady current flows through gated ion channels spanning the plasma membrane of the OS. This "dark current" partially depolarizes the OS of the photoreceptor cell. The photo-activation of the rhodopsin molecules initiates a sequence of reactions that lead to the closure of the cation channels at the membrane, therefore stopping the dark current and causing a potential buildup inside the OS.

The discs positioned first in the path of light will have greater probability of capturing

incident photons and for starting the photochemical process earlier since they are exposed to the incident photons before the other discs. Therefore, the action of each "antecedent" disc on the nearby ion channels will be earlier and greater than the action of each "precedent" disc. Consequently, antecedent cGMP-gated ion channels will show an earlier and greater change in the flow of ionic currents they control and since the OS double-lipid membrane discs are sealed against the passage of ions, the light activated OS will be forming a stack of "almost" isolated solutions each showing a monotonic change in the concentration of ions. Changes in the the ionic channels fluxes are assumed to be greater than the diffusion flows of ions between the inter-discs spacings and which try to reestablish the electrochemical equilibrium. Consequently, a potential difference will exist for a certain amount of time around each disc and the whole OS will behave as a stack of "watch batteries" having the same polarity. The potential difference around each OS discs will increase its refractive index by reorienting the dielectrical dipoles of the double-lipid membrane that forms it. It is worth noting that the solutions with different ionic concentration are not totally isolated since the space between the plasma membrane and the edges of the discs (the two edges in the case of the rod photoreceptor and the one edge in the case of the cone photoreceptor) permit the passage of ions to recreate the electrochemical equilibrium. However, as was highlighted in section 2.2.2, there are experimental evidences that the edges of a rod OS disc are structurally and functionally different than the rest of the disc, and it is possible that some mechanism exists (e.g. disc stretching) to close the pores between the edges and the plasma membrane. The non-existence of such a mechanism does not refute the explanation for discs hyperpolarization outlined in the previous paragraph, but it would indicate that the active action of the high rate cGMP-gated ion channels is countered by the passive diffusion of ions trying to recreate the electrochemical equilibrium. In addition, once the photoreceptor goes back to the dark state, the ionic

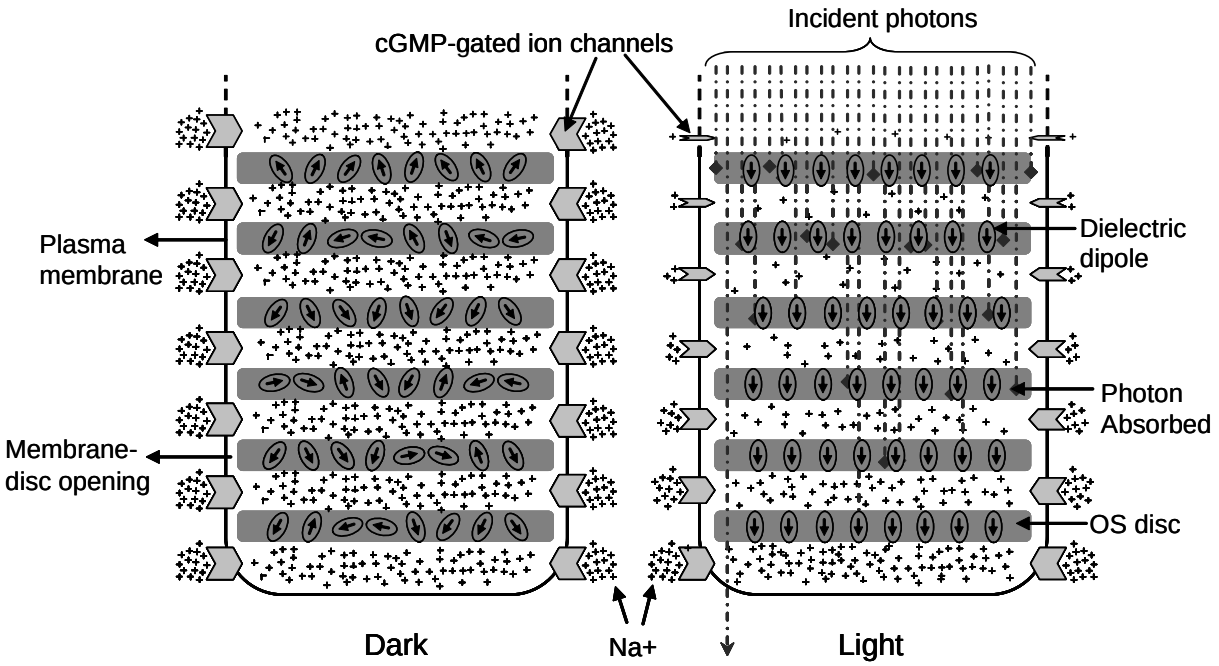

Figure 3.4: Proposed mechanism for light induced hyperpolarization of the OS discs: in dark state, all inter-discs spacing show the same concentration of Na+ ions; in the light state, a concentration gradient exists.

diffusion will slowly reestablish the equilibrium and the refractive index of the discs will decrease back to its original value.

As we will see later in section 4.4, the hyperpolarization of the OS discs is the best candidate process that can explain the increase of reflectivity of the OS. The mechanism presented for OS discs hyperpolarization can be checked experimentally by comparing the differences in the optical signals from rod and cone photoreceptors. The discs in rod OS are free-floating whereas the discs in cone OS stay connected to the plasma membrane at one edge. The rate of reestablishing the electrochemical equilibrium in rod OS will be faster (up to two times) than in the case of cone OS (see fig. 3.5) which might translate as a noticeable difference in the optical functional signal. Based on this hypothesis, it is

Conjectures		
Functional response's parameter	Rod	Cone
Rise time	Slow	Fast
Relaxation Time	Fast	Slow

Table 3.1: Table of testable conjectures spanning from discs hyperpolarization proposed mechanism.

expected that the hyperpolarization of discs in cone photoreceptors should be faster (up to two times) than that of rod photoreceptors. Consequently, the rise time of the OS optical signal in the case of cones will be smaller than in the case of rods. Moreover, the depolarization of discs once the cell is back into the dark state will be faster in rods than in cones. Consequently, the relaxation time of the OS optical signal will be greater in the case of cones than in the case of rods. Currently, the experimental data of the functional response is only available for rod dominated retinal photoreceptors, however, there are some indications that support the first conjecture (see table 3.1) since it is known that rods have slower response to light (they need to be exposed over a certain amount of time to be activated) whereas cones have a quicker response to light (cones can perceive more rapid changes in stimuli) [18].

Structural changes

Light stimulation of a photoreceptor cell can cause structural changes which in turn can affect the light scattering pattern. On light stimulation, the metabolic activity of mitochondria in the IS increases which might cause an increase in its size, density and/or chemical composition and consequently a change in its refractive index [34]. In the OS, the isomerization of the rhodopsin molecules induces conformational changes in the opsin part of the molecules which might cause changes in the size of the discs. In addition, in the light state, the photoreceptor cell and its components might experience swelling due to a change

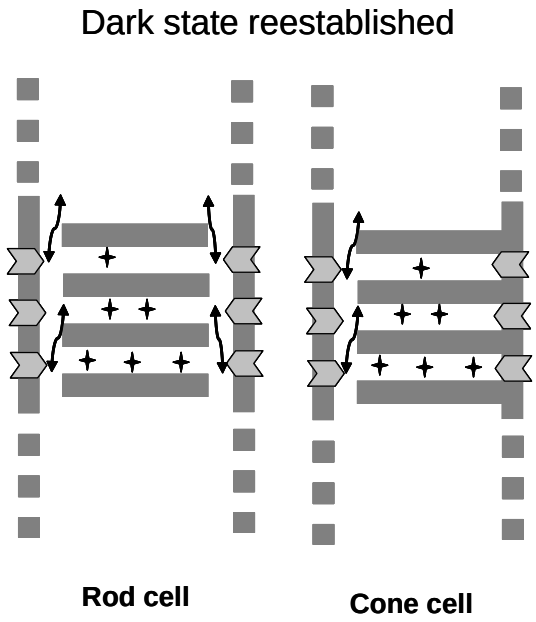

Figure 3.5: Conjectured differences between cone and rod photoreceptors regarding the reestablishment of ionic equilibrium among the inter-discs mediums: the process is faster in rods photoreceptors

in the osmotic pressure which can be attributed to the demanding and fast metabolic activities. Moreover, in bright conditions, a protection mechanism [46] is initiated where the IS of rods elongates to bring the OS closer to the RPE layer and consequently reduce the number of photons absorbed by the OS. The elongation of the IS decreases its aperture at the IS-OS boundary giving the IS a more conical shape. It has been shown [14] that the photoreceptor cell can be modeled as a dielectric light collector which means that the more conical shape of the IS increases its angle of acceptance, which might explain its decreasing reflectivity.

3.5 Conclusions

This chapter presented a general "blue print" FDTD model of the photoreceptor cells. The model was constructed based on the understanding acquired from the literature survey, most of which was presented in chapter 2. Moreover, in this chapter, several hypotheses about the origin of the functional optical signals were presented.

Chapter 4

Simulation Results

4.1 Introduction

In the FDTD simulations, the plane wave excitation had a spectrum spanning $100nm$ around a central wavelength of $1040nm$. These parameters match the properties of the fUHROCT imaging system used in the experiments. For each simulation, scattering profiles were computed for 11 wavelength points ($990nm$, $1000nm$, $1010nm$, ... $1090nm$). Therefore, the dependencies of the tested changes on the signal wavelength can be observed. Moreover, for each test case, a single scattering profile that averages the data of all 11 wavelengths was provided in order to examine the effect of the tested case on the exciting signal over the whole spectrum (a more realistic experimental scenario).

It is worth mentioning that, since the experimental data consists of OCT recording obtained from light scattering measurements over a limited angular range, we are more interested in the light scattering simulation results of the backscattering region and in particular for the range of angles [165°,180°]. Simulation results at lower angles are useful in providing a *priori* understanding of the effectiveness of future light scattering based diagnostic devices.

In the following, the models and the simulation results are presented, starting from the

simple ones to the more complex ones.

4.2 OS Solid Cylinder Model

4.2.1 Description

The thickness of discs, the inter-discs spacing ($\sim 15nm$) and the thickness of the plasma membrane are all "electrically" small compared to the wavelengths of the probing electromagnetic wave. Therefore, as a first step, the OS can be modeled as a solid cylinder with a homogeneous refractive index which encompasses the optical properties of the discs, the cytoplasm (inter-discs spacing) and the plasma membrane. Fig. 4.1 shows a schematic description of the model used. Table 4.1 presents the values of the parameters of the model.

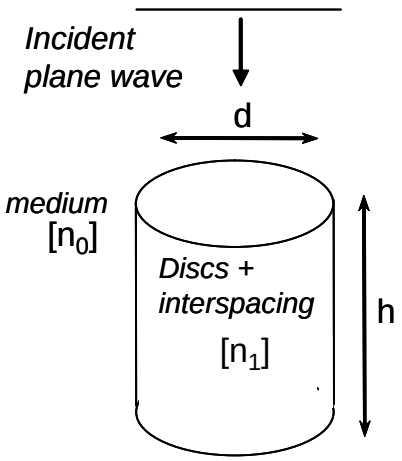

Figure 4.1: Schematic of the OS solid cylinder model showing the model parameters.

4.2.2 Test Cases

Using the solid cylinder model of the OS, the following changes were tested:

Parameter	Symbol	Value
Diameter of inner cylinder	d	$1.56\mu m$
Length	h	$10\mu m$
Medium refractive index	n_0	1.34
Inner cylinder refractive index	n_1	1.41

Table 4.1: Simulations parameters for the solid cylinder model estimated from data in table 2.1.

1. Test case 1: A $\pm 5\%$ change in n_1. This test case models the effect of a change in the refractive index of the OS as a whole on its light scattering pattern. The change in the index of refraction can be attributed to membrane discs hyperpolarization and/or discs hyperpolarizations.

2. Test case 2: A $\pm 10\%$ change in h, the length of the cylinder. This test case models the effect of an elongation or a shortening of a cylindrical structure on light scattering. In the OS, this change can be attributed to the conformal changes in the rhodopsin or to a light protection mechanism. Moreover, the results can be used in the case of the IS where there are experimental evidences about shrinking and elongation of the myoid part as a protection mechanism for excessive lighting conditions.

3. Test case 3: A $\pm 10\%$ change in d, the diameter of the cylinder. This test case models the effect of a change in the "aperture" of a dielectric cylindrical structure on light scattering. In the OS, this change can be attributed to cell swelling which can be caused for example by changes in the osmotic pressure across the plasma membrane. Also, the results can be used in the case of the IS since shrinking and elongation of the myoid is matched with a corresponding change in the aperture.

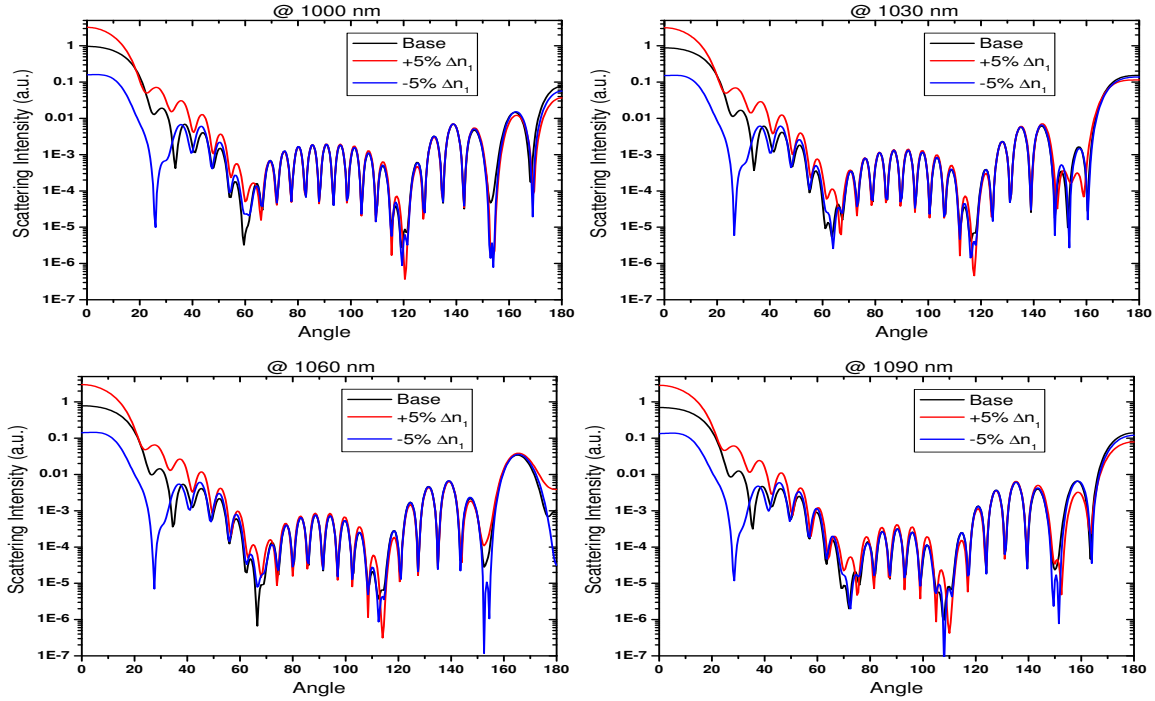

Figure 4.2: Light scattering profiles for a ±5% change in n_1, the refractive index of the solid cylinder (test case 1). a)$\lambda = 1000nm$, b)$\lambda = 1030nm$, c)$\lambda = 1060nm$ d)$\lambda = 1090nm$.

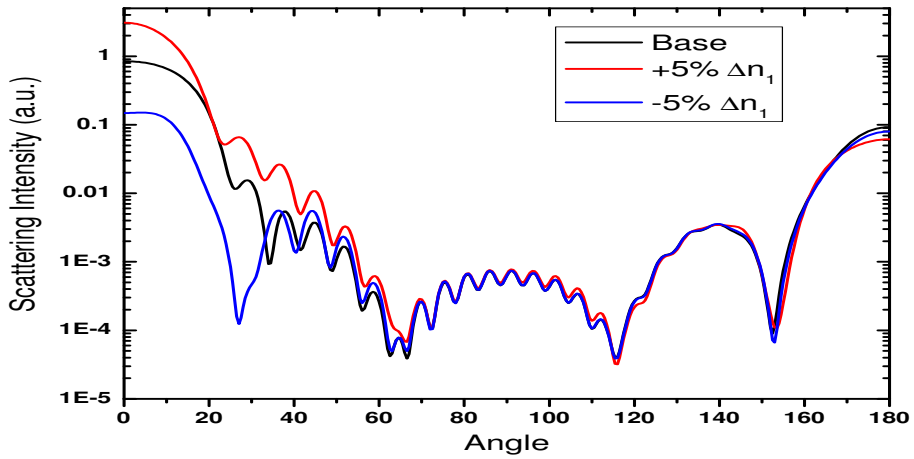

Figure 4.3: Light scattering pattern averaged over the spectrum of the test signal for a ±5% change in n_1, the refractive index of the solid cylinder (test case 1).

4.2.3 Results

Test case 1

Fig. 4.2(a) - 4.2(d) present the scattering profiles for a selection of 4 wavelengths (1000nm, 1030nm, 1060nm and 1090nm) for test case 1. The plots indicate that the effect of changing the refractive index of the solid cylinder on light scattering does not depend on the wavelength of the incident wave. In fact, for all wavelengths, the change in the index of refraction had effect on light scattering in the forward direction (0° to 60°) and a relatively minimal effect on light scattering in the normal direction (60° to 120°) or the backscattering direction (120° to 180°). The independence of the change in light scattering in test case 1 on the wavelength can be checked in fig. 4.3 which averages light scattering profiles for all 11 wavelengths. The plot shows that a 5% increase in the refractive index increases light scattering power in the forward direction and vice versa. No significant changes are observed in the other directions.

Test case 2

Fig. 4.4(a) - 4.4(d) present the scattering profiles for the same selection of 4 wavelengths (1000nm, 1030nm, 1060nm and 1090nm) for test case 2. The plots show that a 10% increase in the length of the cylinder shifts to the right the sidelobes found at angles above 90° and shifts to the left the sidelobes found at angles below 90° and the amount of shift is greater for longer wavelengths. The opposite exactly happens for a 10% decrease in the length of the cylinder.Fig. 4.5 averages light scattering power for all 11 wavelengths. The plot shows that the effect of a change in the length of the cylinder on light scattering has been mitigated for angles higher than 90°. The effect is almost negligible for the angles in the backscattered direction.

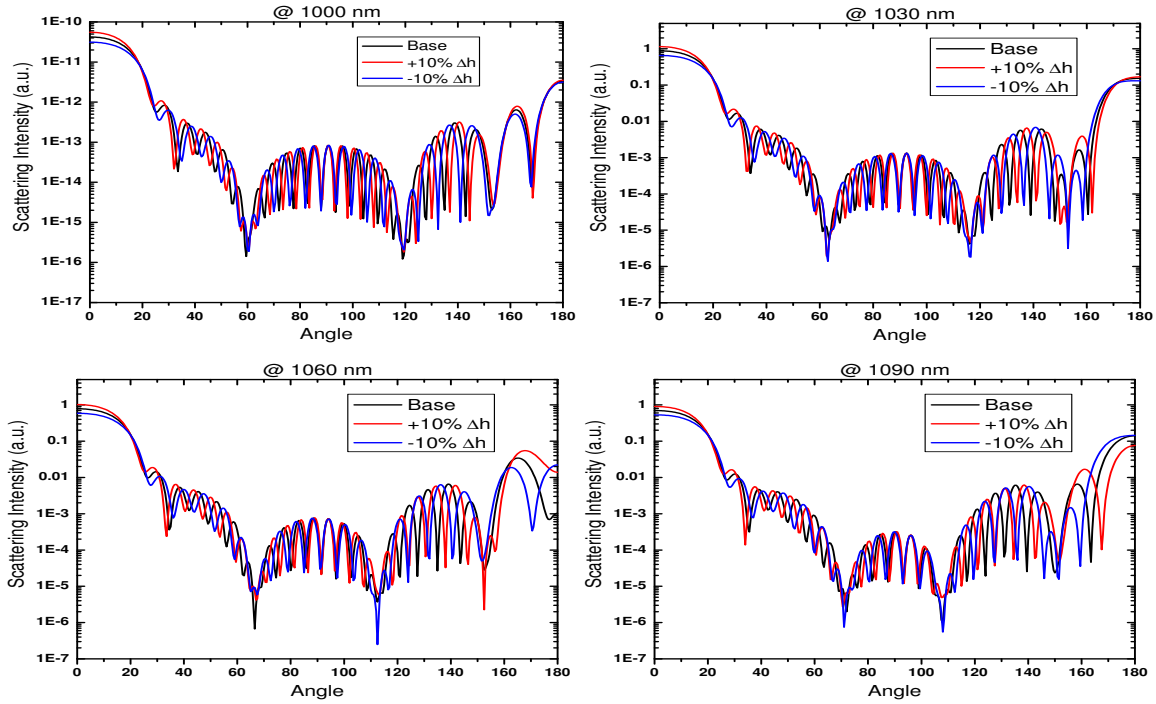

Figure 4.4: Light scattering profiles for a ±10% change in h, the length of the solid cylinder (test case 2). a)$\lambda = 1000nm$, b)$\lambda = 1030nm$, c)$\lambda = 1060nm$ d)$\lambda = 1090nm$.

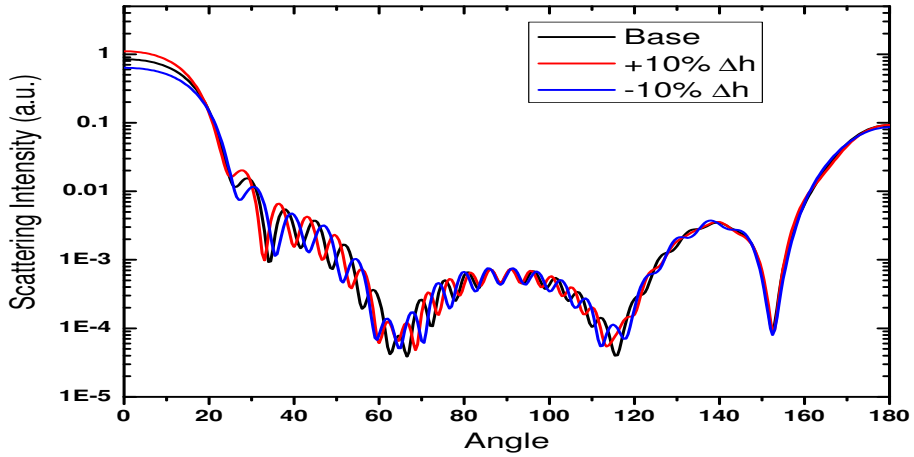

Figure 4.5: Light scattering pattern averaged over the spectrum of the test signal for a ±10% change in h, the length of the solid cylinder (test case 2).

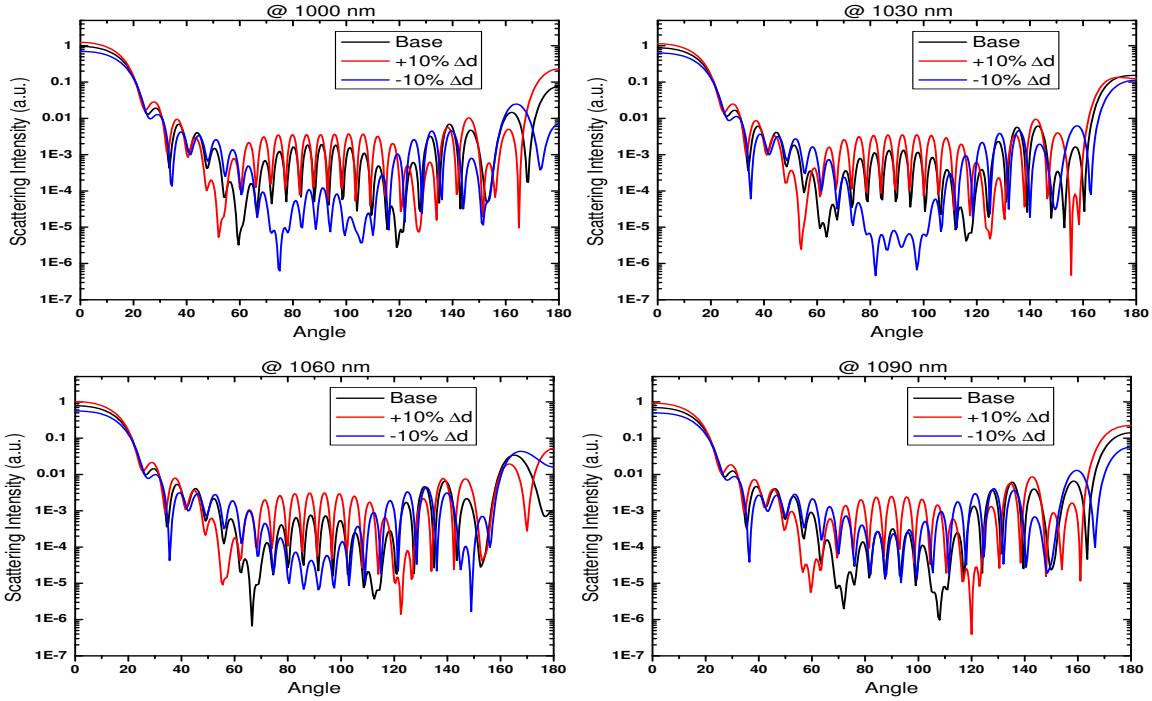

Figure 4.6: Light scattering profiles for a $\pm 10\%$ change in d, the diameter of the solid cylinder (test case 3). a)$\lambda = 1000nm$, b)$\lambda = 1030nm$, c)$\lambda = 1060nm$ d)$\lambda = 1090nm$.

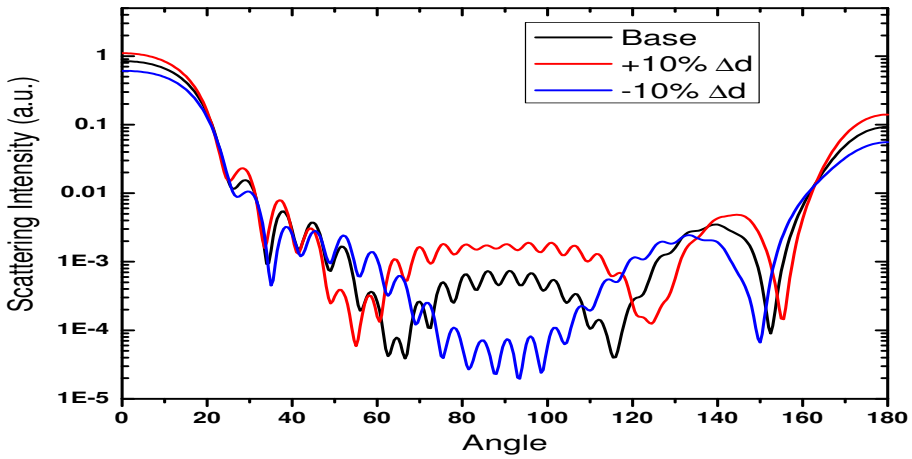

Figure 4.7: Light scattering pattern averaged over the spectrum of the test signal for a $\pm 10\%$ change in d, the diameter of the solid cylinder (test case 3).

Test case 3

The plots in fig. 4.6(a) - 4.6(d) show that changing the "aperture" of the cylinder introduce significant wavelength dependent changes in light scattering profiles especially at angles around the normal direction. The increase in the diameter increases the magnitude of the normal direction sidelobes and vice versa. The effect on the backscattered sidelobes does not follow a specific pattern with the exception for the last sidelobe since its magnitude increases with the increase of the diameter and vice versa. The averaging plot in fig. 4.7 simplifies the analysis since it shows that the increase in the "aperture" of the cylinder increases the magnitude of light scattering of the normal direction sidelobes. The sidelobes in the backscattered become narrower and their magnitudes increase with the increase in the aperture. The change in the magnitude at the backscattered direction is significantly greater than in the previous test cases and therefore it can be used to explain the decrease in reflectivity of the IS as caused by a decrease in its aperture. This decrease in the aperture might be caused by the photoreceptor protection mechanism where the IS elongate when the rod photoreceptor is exposed to external light. The effect of the change is smaller in the forward direction. The opposite happens with a 10% decrease in the diameter.

4.3 OS Double Cylinder Model

4.3.1 Description

In the solid cylinder model, the bulk effect of discs and membrane hyperpolarizations were simulated in a single test case. In order to investigate the effect of membrane hyperpolarization alone, the solid cylinder model was modified by including a thin cylindrical shell representing the outer cell membrane. Fig. 4.8 shows a schematic description of the model

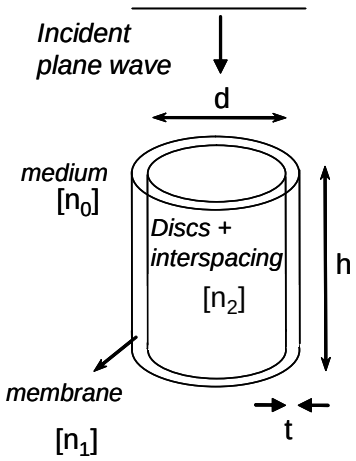

Figure 4.8: Schematic of the OS double cylinder model showing the model parameters.

Parameter	Symbol	Value
Diameter of inner cylinder	d	$1.5\mu m$
Membrane thickness	t	$30nm$
Length	h	$10\mu m$
Medium refractive index	n_0	1.34
Membrane refractive index	n_1	1.48
Inner cylinder refractive index	n_2	1.41

Table 4.2: Simulations parameters for the double cylinder model estimated from data in table 2.1.

used. Table 4.2 presents the values of the model parameters used in the simulations.

4.3.2 Test Cases

Using the double cylinder model of the OS, the effect of a $\pm 5\%$ change in n_1 was tested. This test case models the effect of a change in the refractive index of the outer cell membrane on light scattering. This change in the index of refraction can be attributed to the hyperpolarization of the plasma membrane which occurs during the generation of the neural electrical signal.

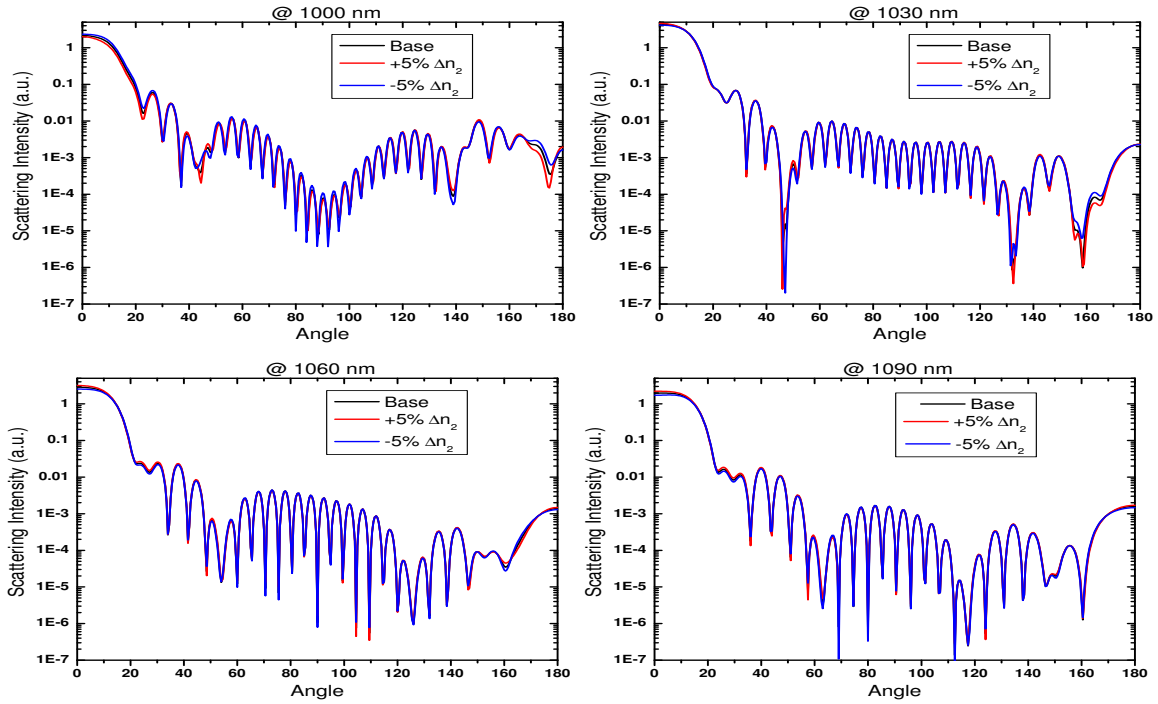

Figure 4.9: Light scattering profiles for a ±5% change in n_2, the refractive index of the cylinder's sheath. a)$\lambda = 1000nm$, b)$\lambda = 1030nm$, c)$\lambda = 1060nm$ d)$\lambda = 1090nm$.

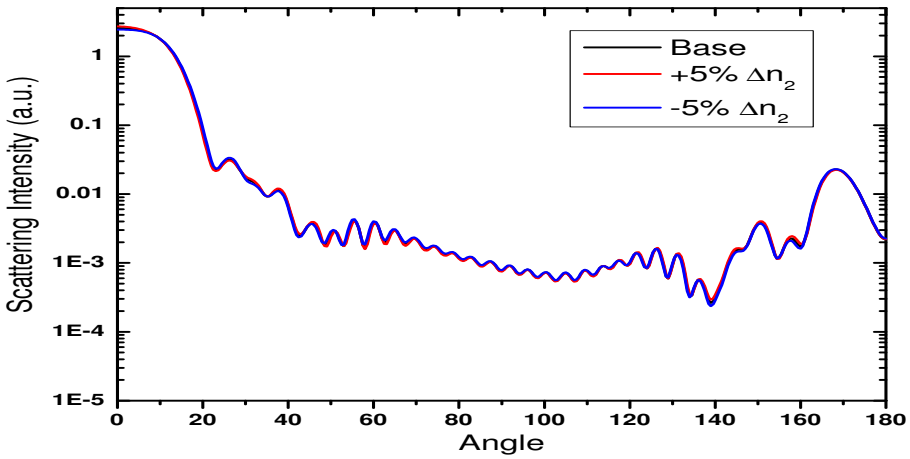

Figure 4.10: Light scattering pattern averaged over the spectrum of the test signal for a ±5% change in n_1, the refractive index of the outer membrane.

4.3.3 Results

As the results in fig. 4.9(a) - 4.9(d) show, a ±5% change in n_1 has a negligible effect on light scattering for all angles and for all wavelengths. The averaging plot shown in fig. 4.10 confirms that membrane hyperpolarization has no significant effect on light scattering. However, when compared with the case of the solid cylinder, modeling the membrane separately has increased the number of sidelobes and reduced the magnitude of light scattering in the normal and backscattered directions.

4.4 OS Discs Stack Model

4.4.1 Description

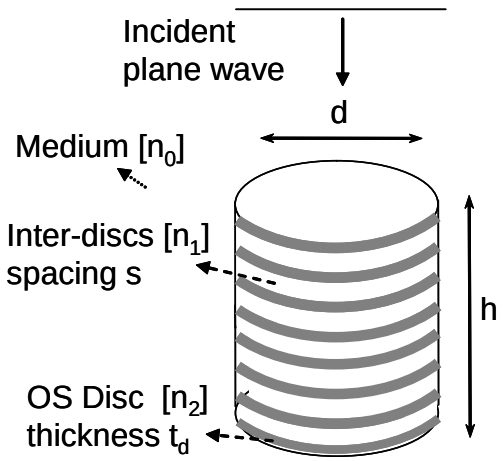

Figure 4.11: Schematic of the OS discs stack model showing the model parameters.

The periodic dielectric structure of the OS might have an effect on light scattering even though the discs thickness and spacing are much smaller than the wavelengths of interests. Therefore, the inner cylinder in the double cylinder model was replaced a by a stack of discs with equal inter-discs separation. Fig. 4.11 shows the disc stack model

Parameter	Symbol	Value
OS diameter	d	$1.5\mu m$
Length	h	$10\mu m$
Disc thickness	t	$15nm$
Inter-Discs spacing	s	$15nm$
Medium refractive index	n_0	1.34
Inter-discs refractive index	n_1	1.37
Discs refractive index	n_2	1.46

Table 4.3: Simulations parameters for the discs stack model estimated from data in table 2.1.

of the OS which contains 333, $15nm$ double-lipid membrane discs separated by $15nm$ cytoplasmic gaps. This 50% duty cycle in the periodicity of the discs stack model was selected after inspection of high magnification images of the OS obtained using scanning electron microscopy [17, 47].

4.4.2 Test Cases

A discs stack model of the OS can be used to test the following changes:

1. Test case 1: A $\pm 5\%$ change in n_2. This test case models the effect of a change in the refractive index of the discs on light scattering. Such a change in the index of refraction can be attributed to the hyperpolarizations of discs.

2. Test case 2: A $\pm 10\%$ change in t, the thickness of a disc. This test case models the effect of a change in the "duty cycle" of the periodic structure which was initially set to 50%. This change can be attributed to the conformal changes in the axial direction when the rhodopsin is photoactivated. The length of the cylinder h is kept constant.

3. Test case 3: A ±10% change in d, the diameter of the cylinder. This case was simulated in the single cylinder model, but it is possible that a change in the "aperture" of a periodic structure might give different results.

4.4.3 Results

Test case 1

Fig. 4.12(a) - 4.12(d) show that the effect of a change in the refractive index of the discs on light scattering profiles. A 5% increase in the n_2 increases light scattering power by a significant factor for all angles, especially for the ones of the normal and backscattered direction. Although this behavior is present for all wavelengths, some wavelengths experience greater change which can reach approximately 3 orders of magnitude in light scattering power as in fig. 4.12(b). In most light scattering patterns presented in this chapter, one can distinguish two types of sidelobes: sidelobes of great magnitudes that form the envelope of the scattering profile and sidelobes of small magnitudes that modulate the scattering profile. In general, the increase in n_2 should increase the number of sidelobes, mainly the modulating ones, and make them narrower, however, because the near-to-far field transformation computes the far field each 0.5°, therefore the very narrow sidelobes are smeared out leaving the envelope sidelobes. Fig. 4.13 shows the effect for the change in n_2 over the whole spectrum. Contrarily to the effect observed in fig. 4.3, a ±5% change in the refractive index of discs in the periodic nonhomogeneous cylindrical structure, that amounts to an effective change of ±2.5% for the entire volume of the OS, caused significant changes in light scattering as compared to the case of a solid cylinder. The increase in the index of refraction of discs causes an increase in light scattering power over most angles and a smearing of sidelobes especially around the direction of normal scattering. The opposite

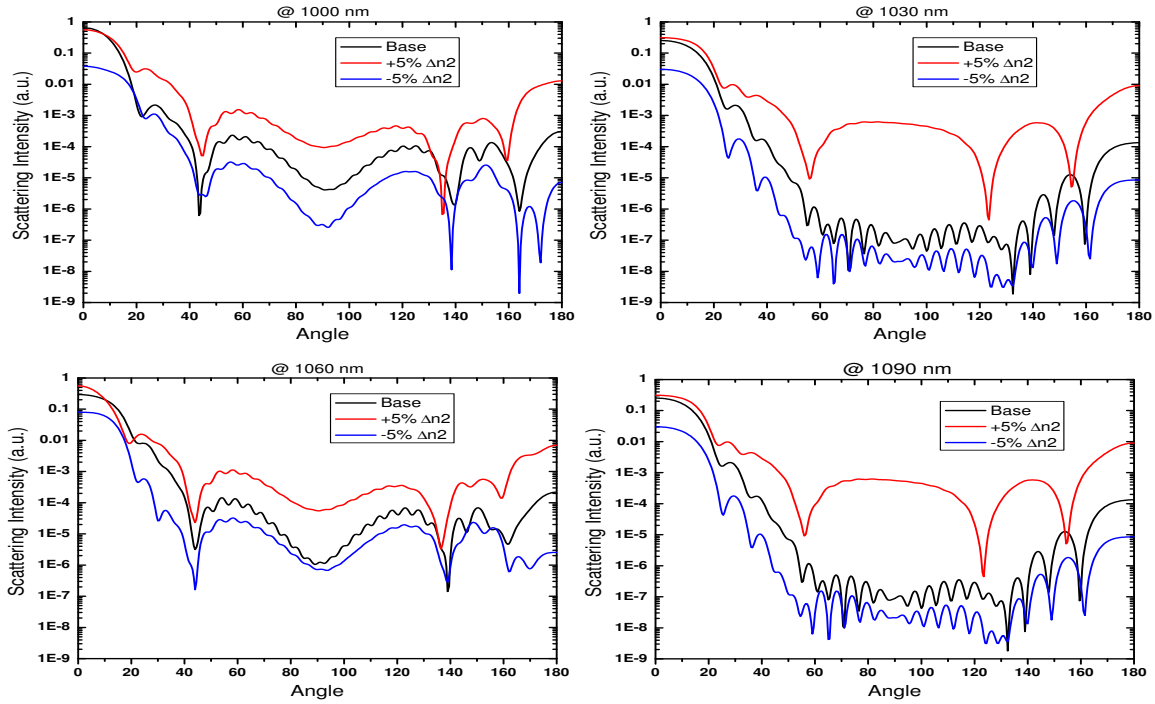

Figure 4.12: Light scattering profiles for a ±5% change in n_2, the refractive index of discs (test case 1). a)$\lambda = 1000nm$, b)$\lambda = 1030nm$, c)$\lambda = 1060nm$ d)$\lambda = 1090nm$.

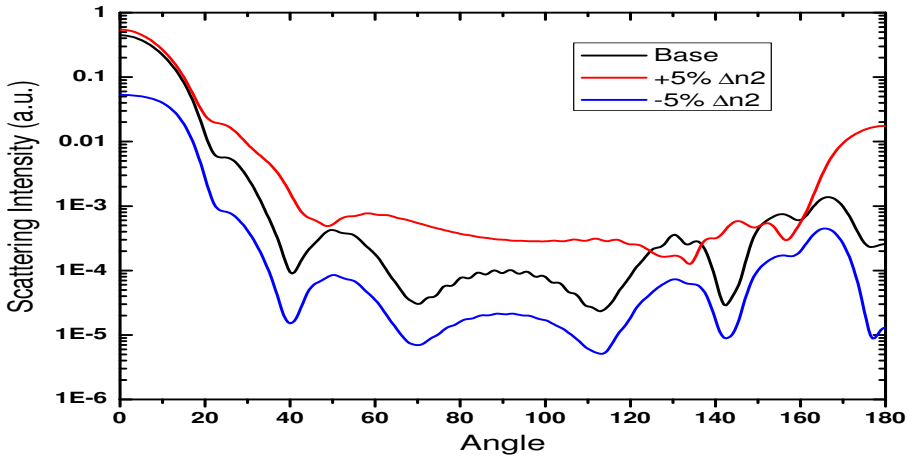

Figure 4.13: Light scattering pattern averaged over the spectrum of the test signal for a ±5% change in n_2, the refractive index of the OS discs (test case 1).

happens with a decrease in the refractive index.

Test case 2

As the results in fig. 4.14(a) - 4.14(d) show, a $\pm 10\%$ change in t, the thickness of discs, has a negligible effect on light scattering for all angles and for all wavelengths. The averaging plot shown in fig. 4.10 confirms that the conformal changes of the rhodopsin along the axial direction has no effect on light scattering.

Test case 3

Fig. 4.16(a) - 4.16(d) present the effect of a $\pm 10\%$ change in the d, the diameter of discs, on light scattering profiles. The effects are most noticeable in the range of 30° to 150°. The increase in the diameter of discs increases the magnitude and numbers of scattering sidelobes around the normal direction and vice versa.

4.5 IS Model

4.5.1 Description

From refractive index data and microscopic images, the volumetric percentage of the mitochondria is estimated at 60% of the ellipsoid volume. For the myoid, the volumetric percentage of the organelles is estimated at 15% of the total volume, again using refractive index data. The IS is modeled as a $12\mu m$ cylinder with 9 mitochondria occupying the lower $7\mu m$ and the rest is occupied by the organelles (160 vacuoles and 40 microtubules). The sizes of mitochondria, vacuoles and microtubules were randomly selected based on ranges found in the literature and their positioning was done randomly while ensuring no

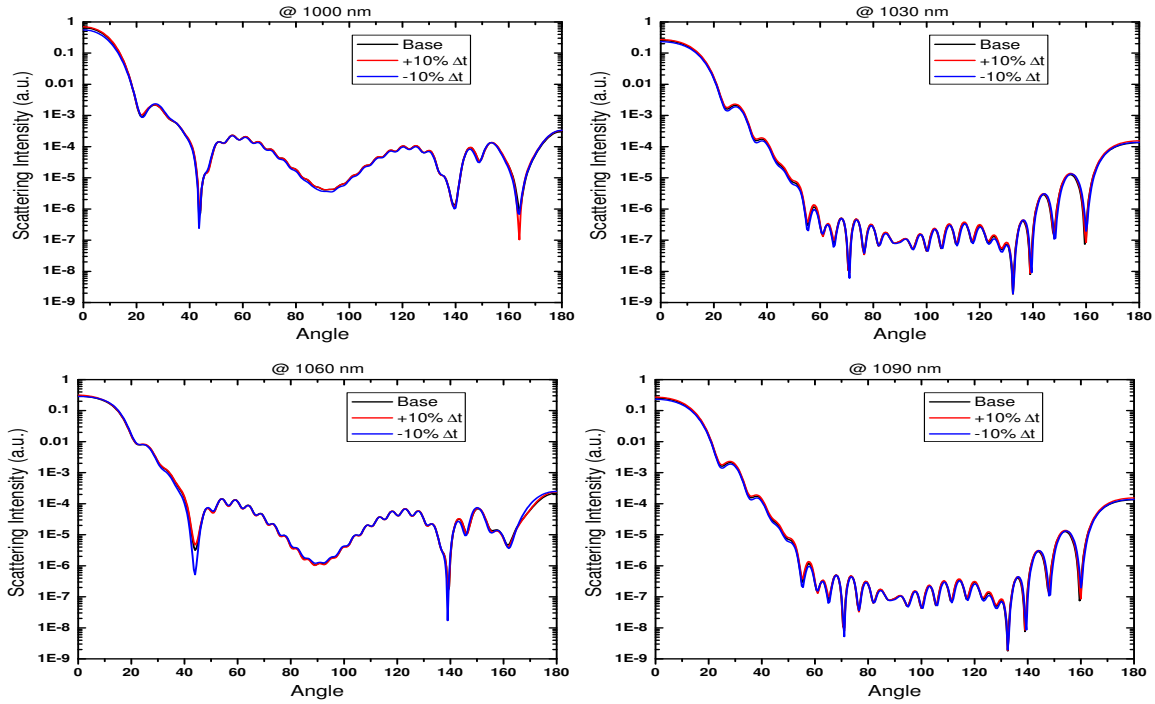

Figure 4.14: Light scattering profiles for a ±10% change in t, the thickness of discs (test case 2). a)$\lambda = 1000nm$, b)$\lambda = 1030nm$, c)$\lambda = 1060nm$ d)$\lambda = 1090nm$.

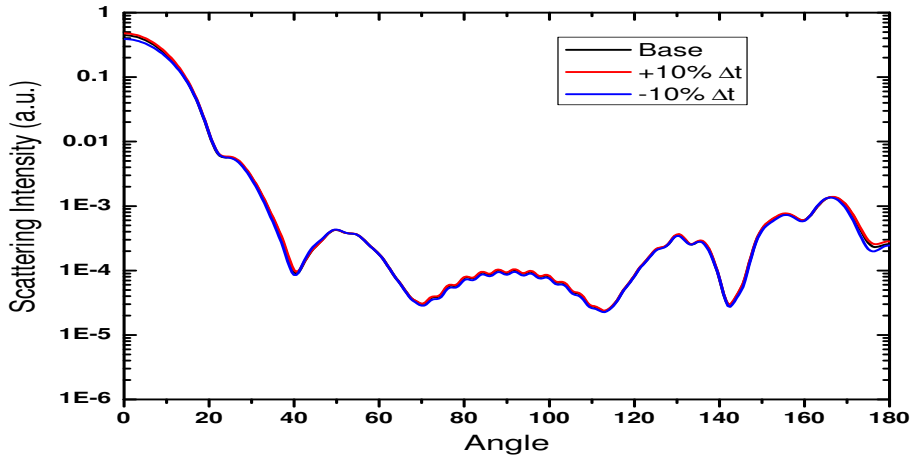

Figure 4.15: Light scattering pattern averaged over the spectrum of the test signal for a ±10% change in t, the thickness of the OS discs (test case 2).

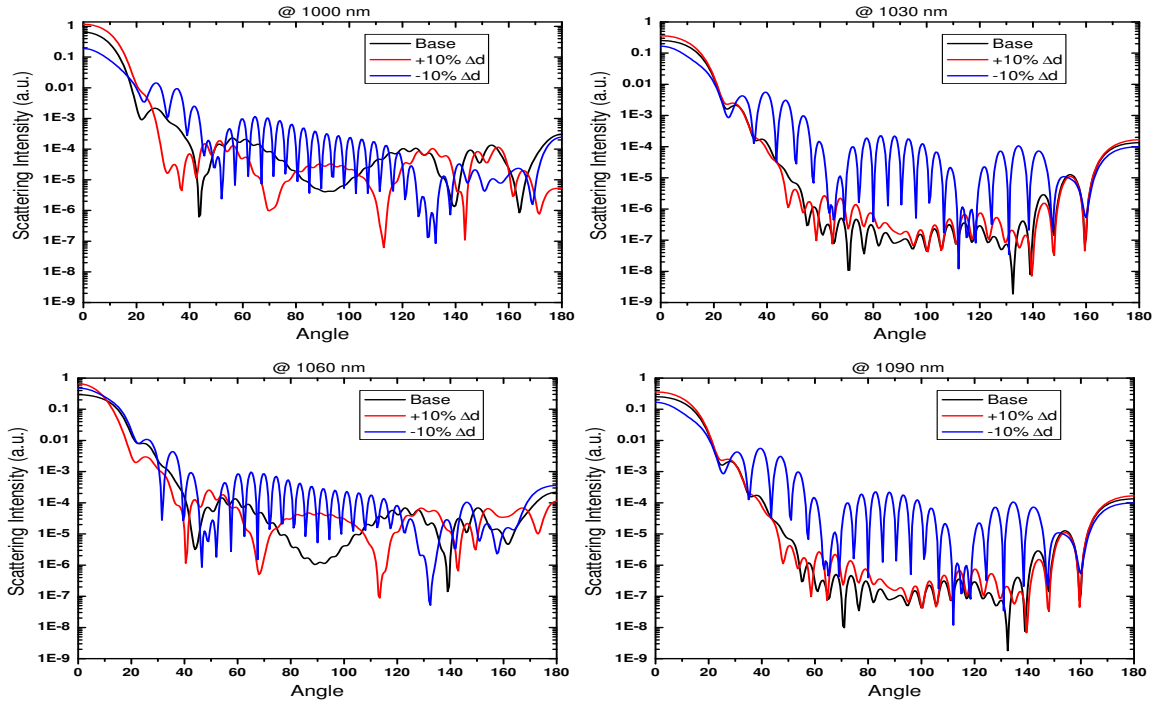

Figure 4.16: Light scattering profiles for a ±10% change in d, the diameter of discs (test case 3). a)$\lambda = 1000nm$, b)$\lambda = 1030nm$, c)$\lambda = 1060nm$ d)$\lambda = 1090nm$.

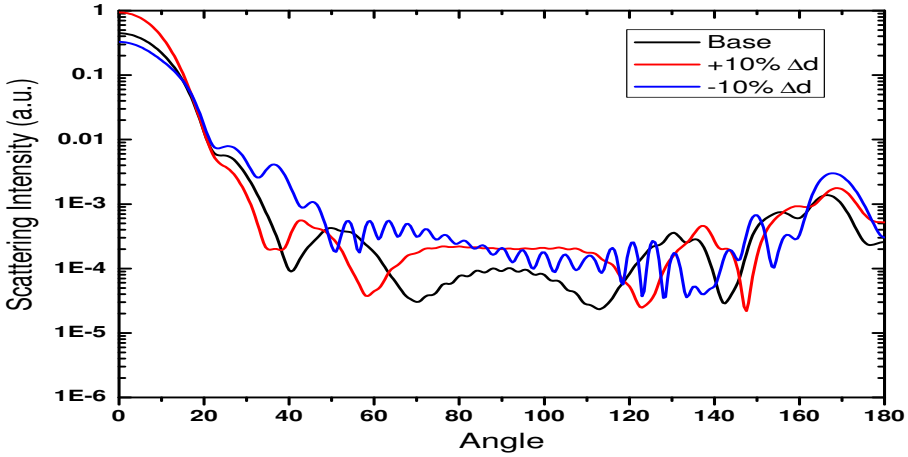

Figure 4.17: Light scattering pattern averaged over the spectrum of the test signal for a ±10% change in d, the diameter of the OS discs (test case 3).

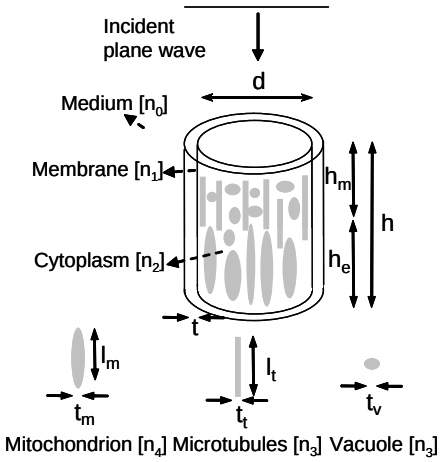

Figure 4.18: Schematic of the IS solid cylinder model showing the model parameters.

intersection. Fig. 4.18 presents a schematic description of the IS model, while table 4.4 indicates the values of the parameters used in the simulations.

4.5.2 Test cases

White light stimulation of a photoreceptor cell increases the metabolic activity of the mitochondria which constitute the bulk of the ellipsoid part of the IS. The effect of the increased metabolic activity on light scattering can be modeled by changes in the structural and optical properties of the mitochondria. Using the IS model, the following changes have been tested:

1. Test case 1: A $\pm 5\%$ change in n_4, the refractive index of a mitochondrion.

2. Test case 2: A $\pm 21\%$ change in v_m, the volume of a mitochondrion.

Parameter	Symbol	Value
Diameter of inner cylinder	d	$1.5\mu m$
Membrane thickness	t	$30nm$
IS length	h	$12\mu m$
Myoid length	h_m	$5\mu m$
Ellipsoid length	h_e	$7\mu m$
Vacuole thickness	t_v	$20 - 80nm$
Microtubule thickness	t_t	$10 - 40nm$
Microtubule length	l_t	$1.5 - 4.5\mu m$
Mitochondrion thickness	t_m	$175 - 250nm$
Mitochondrion length	l_m	$3 - 4.5\mu m$
Medium refractive index	n_0	1.34
Membrane refractive index	n_1	1.48
Cytoplasm refractive index	n_2	1.37
Microtubules & Vacuoles refractive index	n_3	1.42
Mitochondria refractive index	n_4	1.43

Table 4.4: Simulations parameters for the IS model estimated from data in table 2.1.

4.5.3 Results

Test case 1

Fig. 4.19(a) - 4.19(d) show the results of a $\pm 5\%$ change in the refractive index of the mitochondria. Changes in the scattering profile common to all wavelengths occurs at the angles of the forward direction where, in general, the increase in the index of refraction causes a slight increase in light scattering power. Some wavelengths specific changes in scattering power are observed in some sidelobes occurring in the normal and backscattered regions. The average plot in fig. 4.20 indicate that the increase in the refractive index of the mitochondria leads to a small noticeable change in light scattering power in the forward direction. This behavior can be explained by comparing a mitochondrion to an optical fiber and therefore, the increase in the index of refraction causes more light to channel through the mitochondrion in the forward direction.

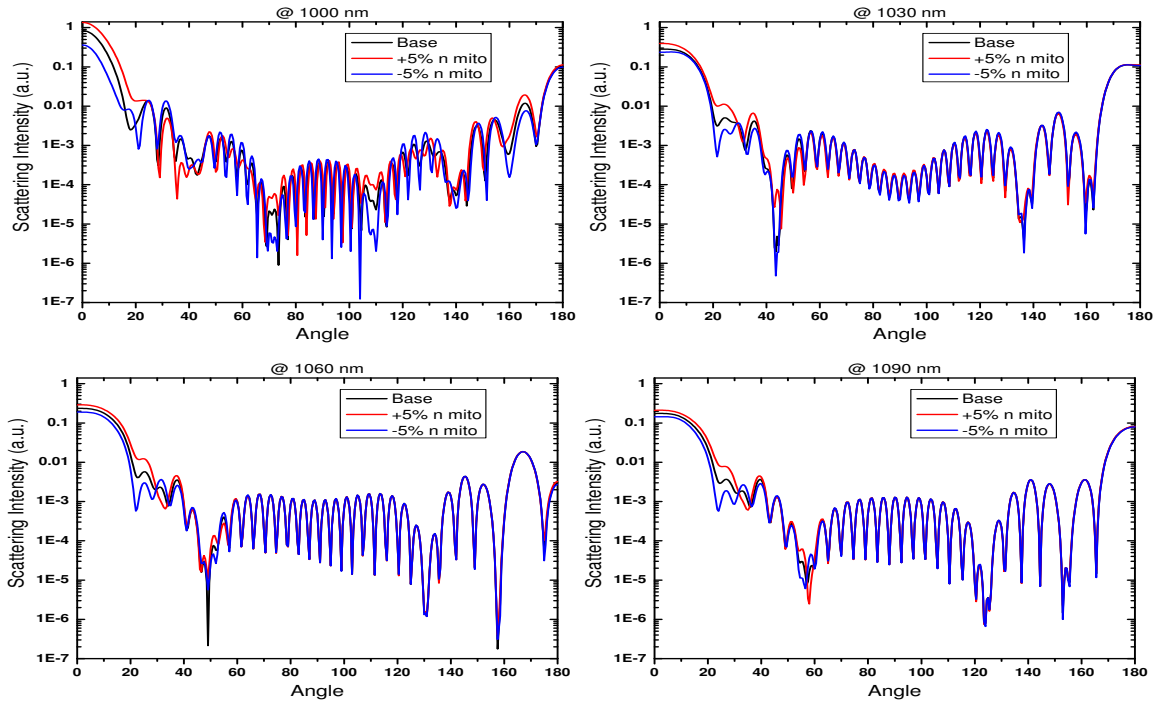

Figure 4.19: Light scattering profiles for a ±5% change in n_4, the refractive index of mitochondria (test case 1). a)$\lambda = 1000nm$, b)$\lambda = 1030nm$, c)$\lambda = 1060nm$ d)$\lambda = 1090nm$.

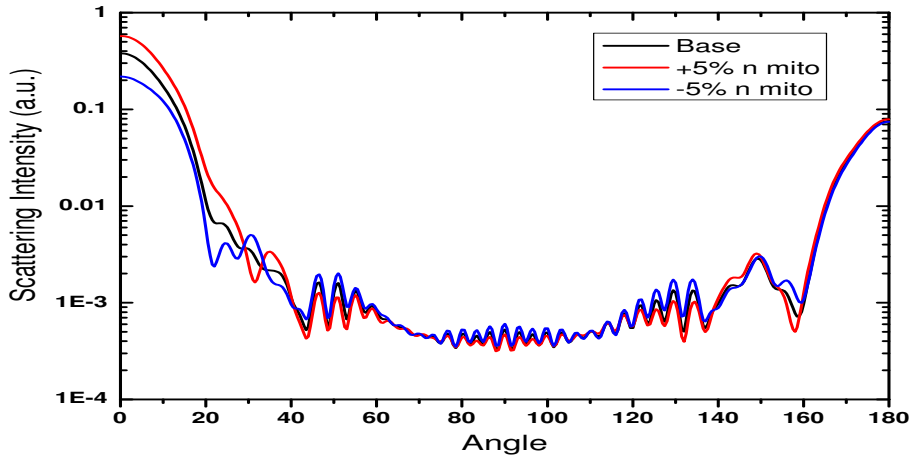

Figure 4.20: Light scattering pattern averaged over the spectrum of the test signal for a ±5% change in n_4, the refractive index of mitochondria (test case 1).

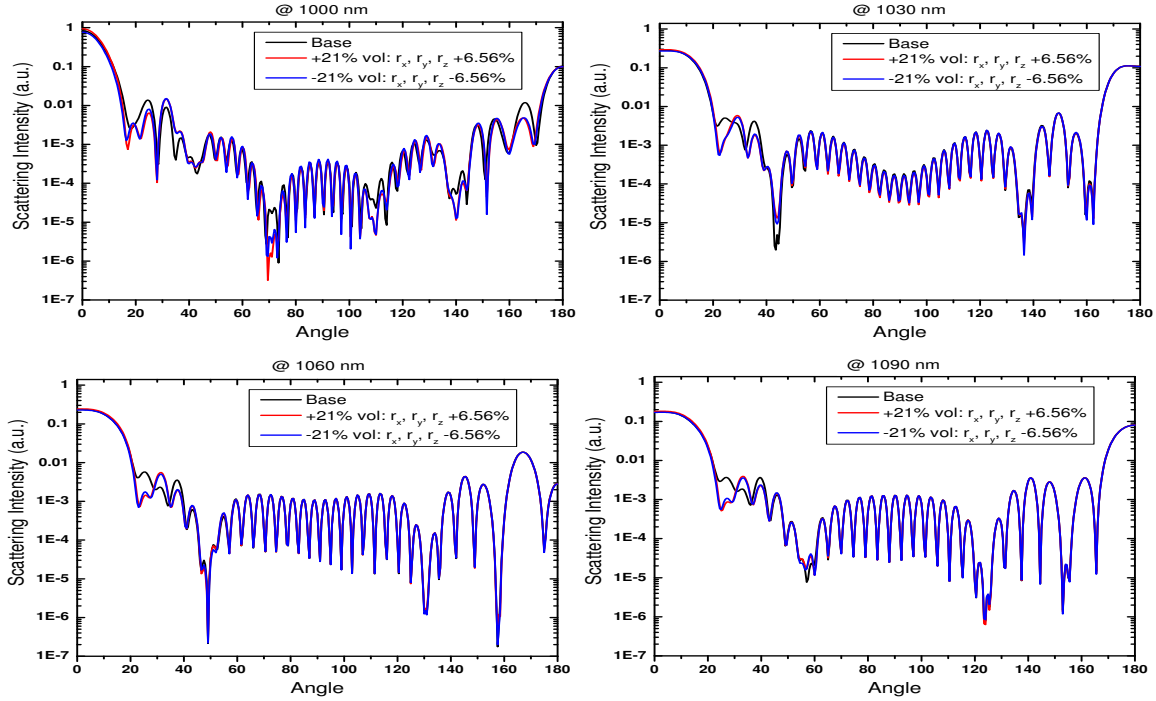

Figure 4.21: Light scattering profiles for a $\pm 21\%$ change in v_m, the volume of mitochondria (test case 2). a)$\lambda = 1000nm$, b)$\lambda = 1030nm$, c)$\lambda = 1060nm$ d)$\lambda = 1090nm$.

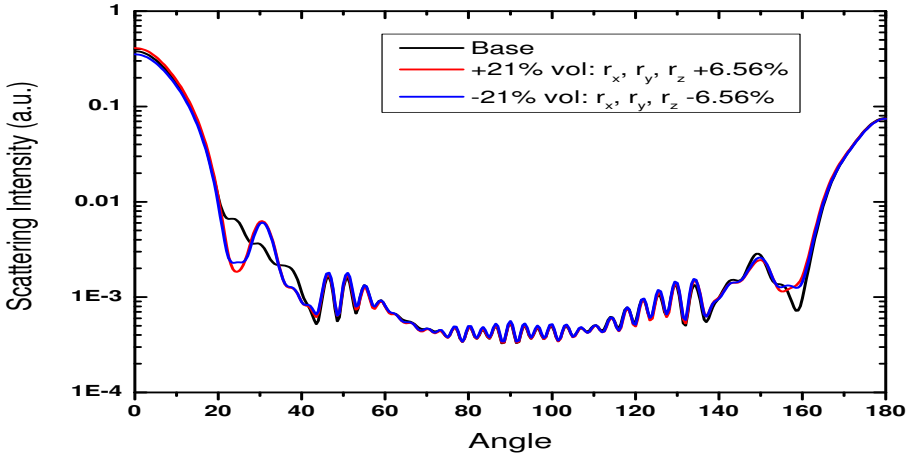

Figure 4.22: Light scattering pattern averaged over the spectrum of the test signal for a $\pm 21\%$ change in v_m, the volume of mitochondria (test case 2).

Test case 2

The change in the volume was selected to be 21% to compare with the case of a 10% change in the lateral thickness (not reported) of mitochondria which causes a change of 21% in the volume in the lateral direction. both cases show identical results. The effect of mitochondria structural changes on light scattering are presented in fig. 4.21(a)-4.21(d). For all wavelengths, the only noticeable changes are seen over the range of angles 20° to 40°. The average plot in fig. 4.22 shows that a ±21% change in the volume of mitochondria has limited effect on light scattering. This means that even with a significantly large change in the volume, the mitochondria still fall in the same regime of light scattering from small objects.

4.6 Conclusions

In this chapter, various FDTD models of the OS and IS were presented. Also, for each model, several test cases were devised. Among all the simulation results obtained, only two cases showed interesting results which can explain the functional response of the photoreceptors. The first case is the ±10% change in the "aperture" as was simulated in test case 3 of the solid cylinder model. For this case, the scattering profile shown in fig. 4.7 indicates appreciable change in light scattering power at the backscattered region, especially at the range of angles [165°, 180°] for which the experimental data were obtained. This result can explain the decrease in the reflectivity of the IS as a change in the "aperture" which can be attributed to the elongation of the myoid during the activation of the protection mechanism or as a cell swelling behavior caused by the high metabolic activity that accompanies the transduction of the neural signal. The second case is the change in the discs index of refraction index n_1 within the discs stack model. This ±5% change

lead to a significant change in light scattering power over all angles and for all wavelengths (fig. 4.12 and fig. 4.13). In particular, the increase in power at the near 180° by more than an order of magnitude can explain the optical response of the OS as caused by the hyperpolarization of discs. On the other hand, results from the rest of models and test cases showed very small variations in light scattering power at the backscattered direction. While no claim can be made on the exclusiveness of the two best results in explaining the functional response, the whole study narrows down the cases of structural changes to changes affecting the "aperture" and the cases of refractive index changes to cases with "high frequency" variation in the static component of the refractive index.

Chapter 5

Numerical Dispersion

5.1 Introduction

5.1.1 Motivation

When compared to the exact physical solution, the FDTD results suffer from phase errors that originate from the discrete nature of the FDTD algorithms. The phase errors strongly depend on the ratio of wavelength to the grid meshing size, especially in the case of second order accurate FDTD. Therefore, the effect of the errors on a propagating signal matches the effect of propagation in a dispersive material, and consequently, the term "numerical dispersion" was coined for this class of errors. In general, reducing the effect of numerical dispersion is constrained by the computational resources and the size of the problem since halving the phase errors requires the doubling of the resolution (i.e. doubling the mesh size in all directions). The main trade-off is between computational resources and accuracy. Moreover, numerical dispersion is more severe in electrically large structures which spans several wavelengths since the error in phase can accumulate up to a 180° phase reversal

during the propagation in the space-time coordinate system.

5.1.2 Objectives

To our knowledge, there hasn't been any study which quantifies the effect of numerical dispersion on light scattering profiles obtained using the FDTD approach outlined in chapter 3. Consequently, the meshing step in all simulation jobs performed during this study was reduced in order to achieve the minimum error possible. The disadvantage in this approach is the consumption of large computational resources in terms of memory, processing units, storage and more importantly the waiting time a researcher will have to spend for maybe a simple first round simulations. In this chapter, a study of the effect of numerical dispersion in light scattering simulations is presented. The main objective is to provide quantitative data about the nature and magnitude of errors introduced in the scattering profiles for a given mesh size. This a *priori* understanding will allow better productivity in applying FDTD for scattering related problems.

5.2 Theory

Numerical dispersion is manifested by the modification of the real wavenumber k to a numerical wavenumber $\tilde{k}$. Eq. 5.1 shows how the wave dispersion equation in FDTD depends on the time step Δt and the mesh step ΔZ. The stability of the FDTD algorithm constrains the Courant factor $C = \frac{v\Delta t}{\Delta Z}$ to be $< \frac{1}{\sqrt{dim}}$ ($< \frac{1}{\sqrt{3}} \approx 0.577$ for 3D simulations). Setting the Courant factor to 0.5, $\tilde{k}$ can be simply expressed as a function of the relative mesh size $\frac{\Delta z}{\lambda}$ (eq. 5.2) and the solution will be stable even for the coarse meshing of $\frac{\lambda}{\Delta Z} = 10$. In the case of sinusoidal waves, the numerical phase velocity can be calculated using eq. 5.3. Fig. 5.1 presents a plot of the ratio of the numerical phase velocity to

theoretical one versus the relative mesh size. The maximum phase error introduced in a structure spanning m number of wavelengths can be calculated using eq. 5.4. Fig. 5.2 shows the phase error introduced in a sinusoidal wave after propagating a distance of 10λ (i.e. $m = 10$).

$$\tilde{k} = \frac{1}{\Delta Z} \arccos\{1 + (\frac{\Delta Z}{c\Delta t})^2[\cos(\omega\Delta t) - 1]\} \tag{5.1}$$

$$\tilde{k} = \frac{1}{\Delta Z} \arccos\{1 + 4[\cos(2\frac{\Delta Z}{\lambda}) - 1]\} \tag{5.2}$$

$$\tilde{\nu_p} = \frac{\omega}{\tilde{k}} = \frac{2\pi f}{\frac{1}{\Delta Z} \arccos\{1 + 4[\cos(2\frac{\Delta Z}{\lambda}) - 1]\}} = \{\frac{\frac{\Delta Z}{\lambda}}{\arccos\{1 + 4[\cos(2\frac{\Delta Z}{\lambda}) - 1]\}}\}\nu_p \tag{5.3}$$

$$\Delta\phi = m\lambda\frac{\Delta Z}{\lambda}(1 - \frac{\tilde{\nu_p}}{\nu_p}) \times 360^\circ \tag{5.4}$$

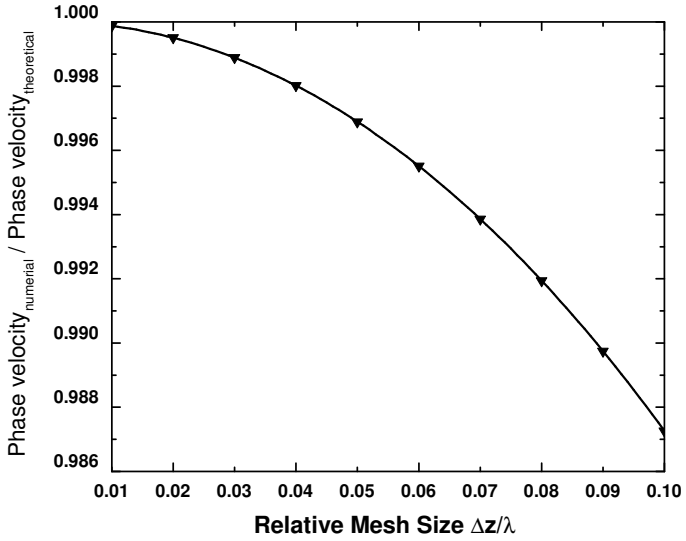

Figure 5.1: Relative numerical phase velocity vs. relative mesh size. The numerical phase velocity is taken relative to the theoretical one.

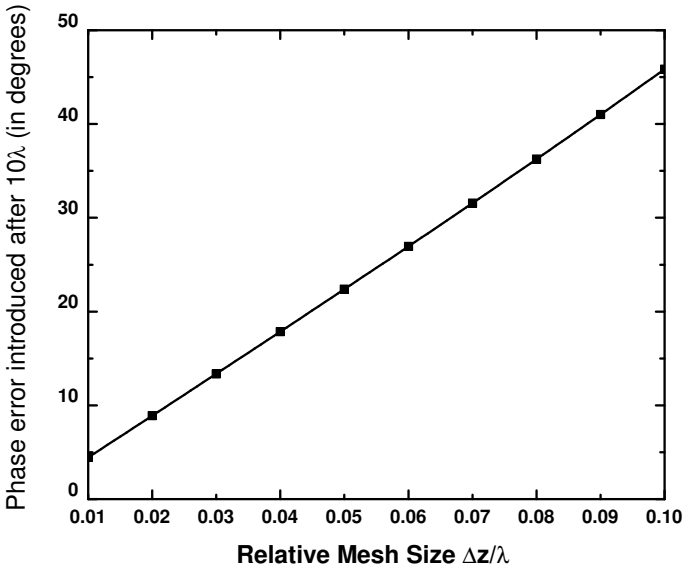

Figure 5.2: Numerical phase error (in degrees) vs. relative mesh size. The error is introduced in the phase of a sinusoidal signal which propagated a distance of 10λ.

5.3 Methods

5.3.1 Overview

In light scattering computations using the FDTD method, there are two processing steps: The first step consists of the FDTD solution of the interaction of an incident wave with a scattering object. At the end of the first step, the near-fields over a surface enclosing the object are stored. The second step consists of the near-to-far field transformation which integrates the contribution of all near-fields at the far zone. Numerical dispersion is introduced in the first step and it has been suggested in [48] that the integration aspect of the near-to-far field transform can mitigate the phase errors, therefore, reducing the weight of the numerical dispersion on the scattering profiles. In investigating the effect of numerical dispersion on light scattering, separate analyses were made for the near and

far-field results.

5.3.2 Model

Our main interest in this study is to quantify the errors in our results. In general, the presence and the value of phase errors in our results do not affect the conclusions drawn since the interest was in the relative change in the scattering pattern rather than in the absoluteness of the results. The quantification of errors will be most useful when the numerical values of the results are needed, for example during a future development of the diagnostic method. Since the photoreceptors were modeled as long cylindrical structures,

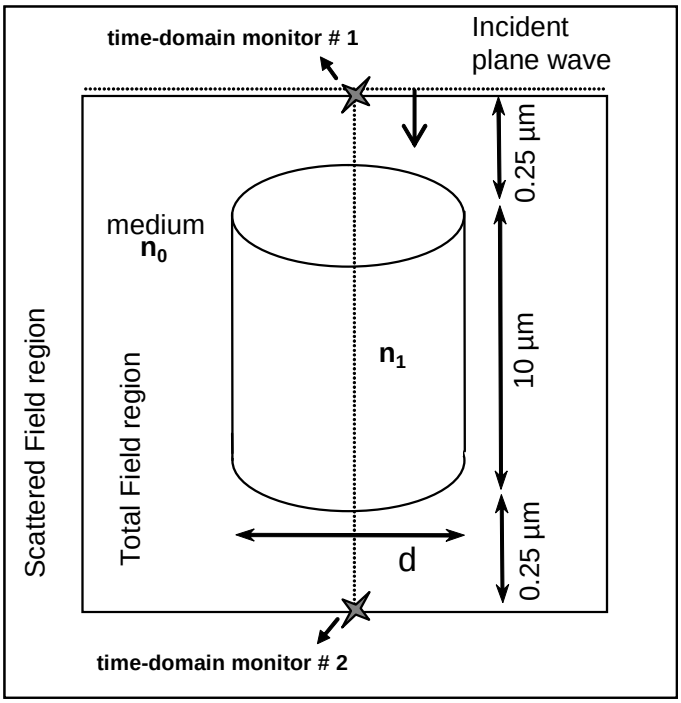

Figure 5.3: The setup of the FDTD simulations for numerical dispersion. The stars show the locations of the time-domain monitors used.

the study of the numerical dispersion was done for the most basic model used, the solid

cylinder model presented in section 4.2. The effect of numerical dispersion on the model was simulated by increasing progressively the mesh size in the axial direction since the incident wave travels for the longest distance and duration in this direction. The incident plane wave pulse has $100nm$ bandwidth around a central wavelength of $\lambda_{cen} = 1\mu m$. The simulations were performed for three cylinders of different diameters ($0.1\mu m$, $1\mu m$ and $5\mu m$). These different apertures are meant to be representative of the three distinct scattering regimes: In the first regime, λ, the wavelength of the excitation is greater than $\sqrt{\sigma}$ where $\sigma = \pi\frac{d^2}{4}$ is the scattering cross section area and d the diameter of the cylinder. In the second regime, λ is comparable to $\sqrt{\sigma}$ and in the third regime, λ is smaller than $\sqrt{\sigma}$ ($\frac{\lambda_{cen}}{\sqrt{\sigma}} \approx 8$, 0.8, 0.16 respectively).

5.3.3 Near-fields analysis method

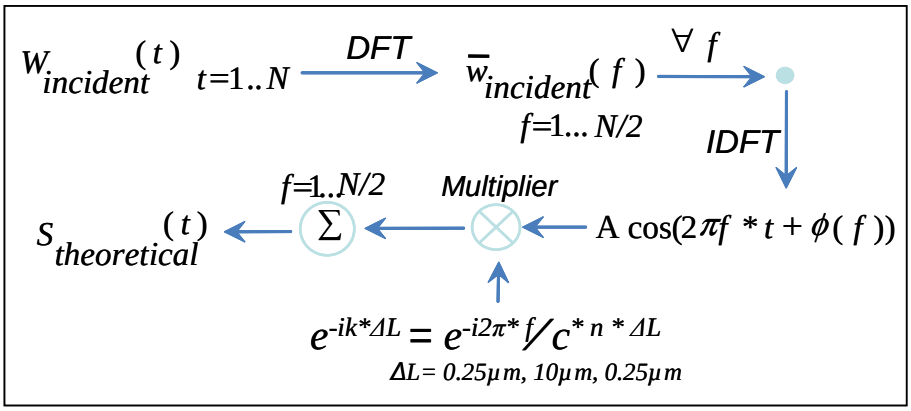

Figure 5.4: Processing flow chart showing the generation of the theoretical signal $S_{theoretical}$ with ideally zero phase error. $S_{theoretical}$ was obtained from an ideal propagation of the incident signal recorded by the first time-domain monitor toward the location of the second time-domain monitor.

The analysis of the near-fields consists of determining the error in phase introduced during the propagation of the plane wave from its insertion point at the TF-SF boundary

to the opposite boundary. Two time-domain point monitors were set along the main axis of the cylinder to record the time signals that will be used in the processing (fig. 5.3). The first Time-monitor records the incident plane wave entering the TF region whereas the second time-monitor records the signals reaching the other end of the TF region. The incident signal recorded by the first time-domain monitor was used to create the propagated incident signal as it should be theoretically at the location of the second time-domain monitor. Fig. 5.4 presents the processing flow used to implement the ideal propagation of the incident signal. A Discrete-Fourier-Transform (DFT) transforms the incident pulse into the frequency domain, then each frequency component is selected and inverse transformed back to the time-domain using Inverse-Discrete-Fourier-Transform (IDFT). The harmonical signal obtained in the previous step is multiplied by the phase factor e^{-kx} where k is the wavenumber corresponding to the frequency f and to the medium of propagation with length ΔL and refractive index n (c is light celerity). Finally, all time sub-signals are integrated to generate the ideally propagated signal $S_{theoretical}$. $S_{theoretical}$ has ideally zero phase error and therefore, the difference in phase when compared to the FDTD signals recorded by the second time-domain monitor approximates the phase error introduced by the numerical dispersion. Fig. 5.5 presents the processing diagram for the computation of phase errors in the FDTD signals. First, the DFT signals of both reference (i.e., theoretical) and target (i.e., simulated) signals were computed to determine the spectrum of interest. Then each frequency component is selected and inverse transformed back to the time-domain using IDFT. The time-domain sub-signals are inputted to the hilbert analyzer which computes the phase difference. The phase difference are reported per each frequency of the source signal spectrum.

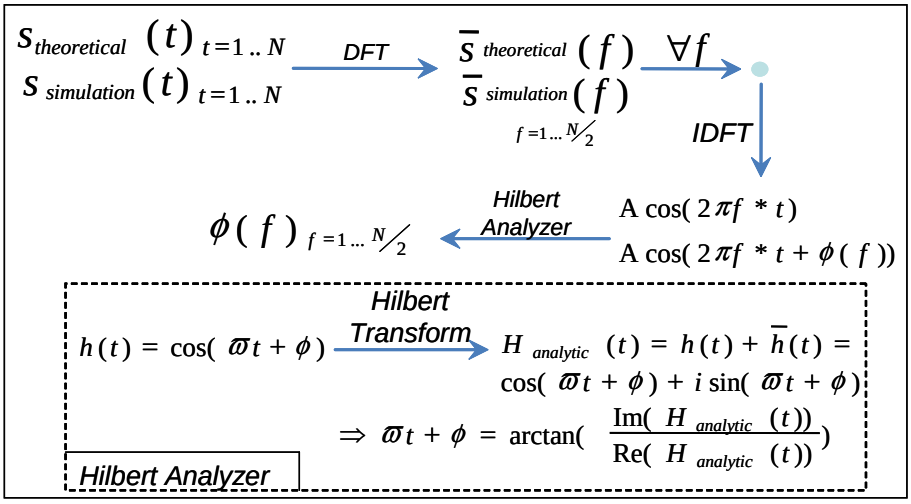

Figure 5.5: Diagram of processing to determine numerical dispersion

5.3.4 Far-fields analysis method

The far-field results consist of scattering profiles computed for each mesh size. The errors can only be reported relative to the case of finest grid since there is no analytical solution for light scattering from a finite cylinder where the incident wave propagates along the axial direction.

5.4 Results

5.4.1 Near-field results

Fig. 5.6 shows the phase error introduced in the near-fields data after propagating through the TF region. The figure shows that, as the mesh size increases, the phase error at the smaller wavelengths starts to increase at a faster rate compared with the errors at the longer wavelengths. For relative mesh sizes $\frac{\lambda}{\Delta Z} > 0.02$, this difference in phase error can pass the 200%.

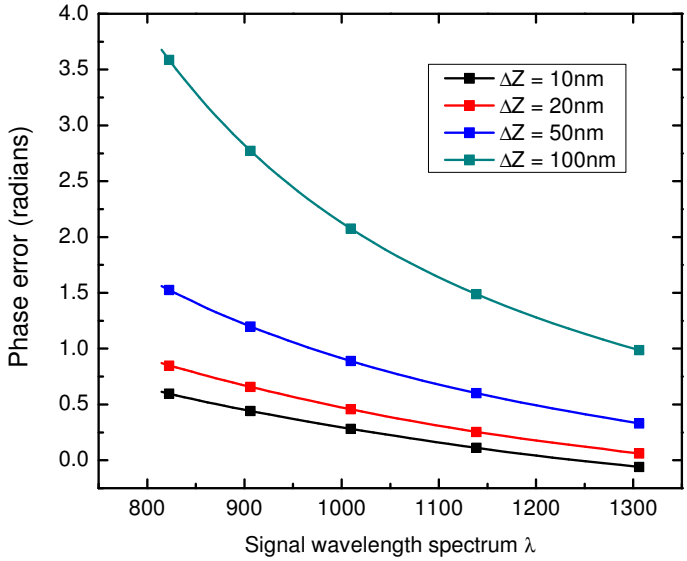

Figure 5.6: Phase error plotted vs. signal wavelength spectrum for various mesh sizes ($\frac{\Delta Z}{\lambda}$=0.01, 0.02, 0.05 and 0.1).

Fig. 5.7 presents the phase error occurring at the median wavelength with peak power ($\lambda = 1000nm$). The result compares well with the theoretical phase error calculated for the same wavelength and presented in fig. 5.1. Also, fig. 5.7 shows that for a structure of 10λ, the error in phase in the near-fields is less than 180° for most practical meshing sizes and less than 90° for mesh size satisfying $\frac{\Delta Z}{\lambda} < 0.06$. Fig. 5.8 presents the ratio of the average phase velocity of the propagated signal. The results show significant deviations and faster decrease as a function of the mesh size when compared with phase velocity values reported by the theoretical analysis (see fig. 5.1). The analysis of the effect of numerical dispersion on near-fields showed that the phase error will not exceed 90° for mesh size satisfying $\frac{\Delta Z}{\lambda} < 0.05$. Also, over a spectrum of $100nm = \frac{\lambda_{central}}{10}$, the variation in phase error will not exceed 60°, again for mesh sizes $\frac{\Delta Z}{\lambda} < 0.05$. Above these thresholds, the variations show a deviation from the linear behavior where the phase error can change by values up to 180°. In terms of phase velocity, the change is less or equal to 5% for mesh

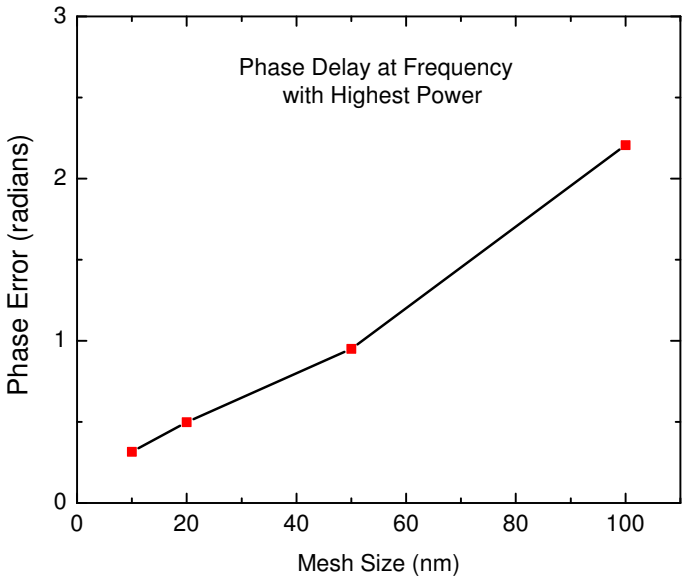

Figure 5.7: Phase error at median spectrum wavelength (with highest power) plotted vs. mesh sizes ($\frac{\Delta Z}{\lambda}$=0.01, 0.02, 0.05 and 0.1).

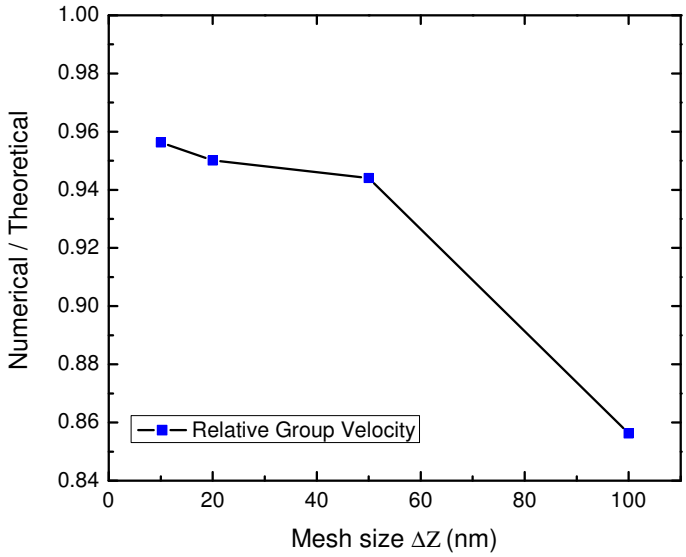

Figure 5.8: Ratio of average phase velocity to the theoretical phase velocity plotted vs. mesh sizes ($\frac{\Delta Z}{\lambda}$=0.01, 0.02, 0.05 and 0.1).

size satisfying $\frac{\Delta Z}{\lambda} < 0.05$ and can reach 15% for mesh size satisfying $\frac{\Delta Z}{\lambda} = 0.1$.

5.4.2 Far-field results

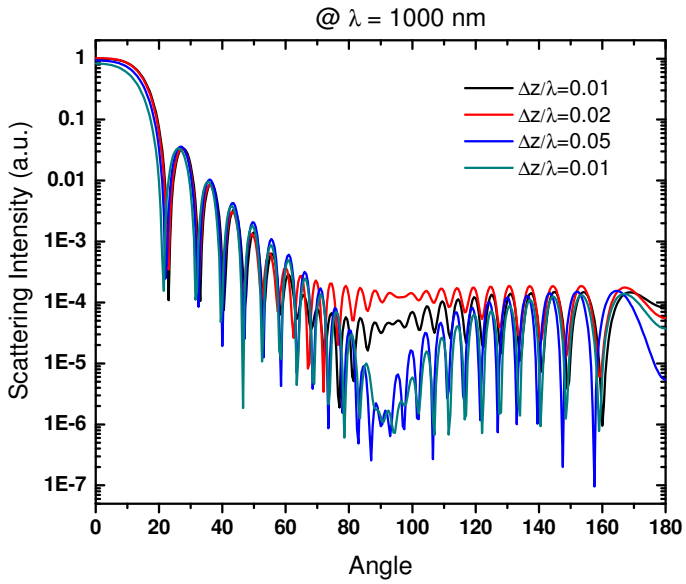

Figure 5.9: Effect of numerical dispersion on light scattering in the case of small scattering cross section as compared to the wavelength (case 1).

The far-field results are reported for the three regimes of scattering as explained earlier. Fig. 5.9 shows the light scattering profile for the first regime, where the wavelengths of the signal are much greater than the diameter of the cylinder. In this case, numerical dispersion has the greater effect around the normal scattering directions where the sidelobes experience large fluctuations in their magnitude. The sidelobes in the forward and backscattering directions show a slight shift towards lower angles. Fig. 5.10 presents the light scattering profile for the second regime of scattering where the diameter of the cylinder is comparable to the wavelengths of the signal. In this regime, the sidelobes around the normal directions start to show less magnitude fluctuations and more positional fluctua-

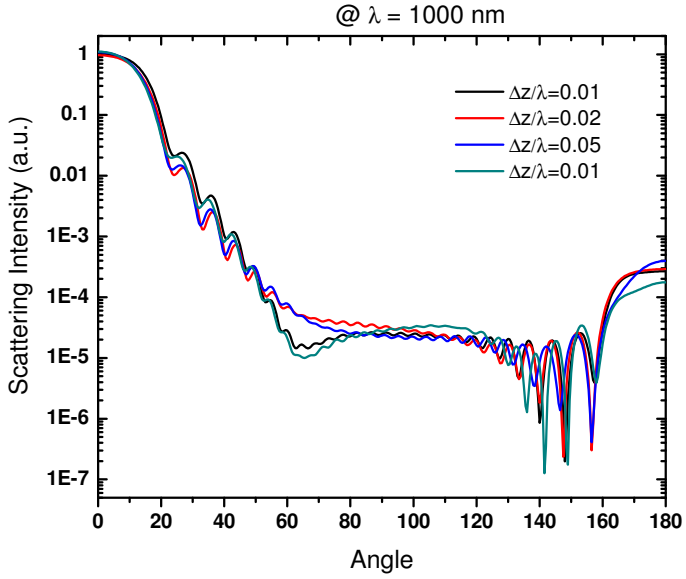

Figure 5.10: Effect of numerical dispersion on light scattering in the case of medium scattering cross section as compared to the wavelength (case 2).

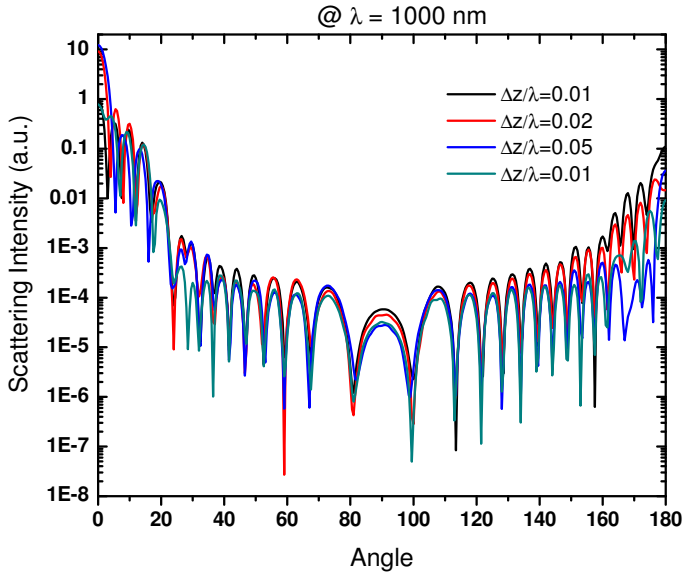

Figure 5.11: Effect of numerical dispersion on light scattering in the case of large scattering cross section as compared to the wavelength (case 3).

tions whereas the opposite happens in the normal and backscattered directions. Fig. 5.11 presents the light scattering profile for the third regime of scattering where the diameter of the cylinder is larger than the wavelengths of the signal. In this regime, the sidelobes around the normal directions show slight variations in magnitude whereas the sidelobes of the backscattered and forward regions show a mix of large magnitude and positional changes.

5.5 Conclusion

We have investigated the effect of numerical dispersion on light scattering profiles obtained from simulations of retinal photoreceptors models. The near-field results quantified the maximum phase error and the relative phase velocity observed versus the meshing size. Far-field results show that numerical dispersion either affects the sidelobes in forward and backscattering regions or the sidelobes in the normal scattering directions. The normal direction sidelobes are less affected as the aperture increases whereas the opposite happens for the sidelobes of the forward and backscattering regions.

Chapter 6

Conclusions

6.1 Summary

We have simulated changes in light scattering from retinal photoreceptors evoked by external light stimulations. Various physiological processes have been investigated such as double-lipid membrane and discs hyperpolarization and cell structural changes. Their effect on light scattering has been determined. Simulation results indicate that OS discs hyperpolarization is the most likely cause for the increase of optical reflectivity from the OS. Other results suggest that the decrease in optical reflectivity of the IS is due to the elongation of the IS which acts as a protection mechanism from excessive lighting conditions. These results will be compared with experimental fUHROCT data acquired from animal models and human studies. We hope that the comparison of experimental and computational results would provide conclusive indications as to how different light induced physiological processes in the retina affect the detected fUHROCT signal. Such analysis will be crucial for the future development of fUHROCT as an ophthalmic diagnostics tool for neurodegenerative diseases, comparable and complementary to ERG.

In addition, we have investigated the effect of numerical dispersion on light scattering profiles obtained from simulations of retinal photoreceptors models. The study shows that numerical dispersion have different effects for various scattering regimes. The study indicates that the conclusions drawn from the photoreceptors simulations are not affected by the values of errors presents in the results.

6.2 Future Work

The work described in this thesis has paved the way for further investigations on the effect of physiological processes on light scattering from photoreceptors. We hope to increase the accuracy of the models to be able to use the quantitative aspects of the results in order to compare with the experimental results. Also, the work suggested couple functional imaging experiments to validate the explanation of the mechanisms leading to OS discs hyperpolarization. In addition, there is a need for an understanding of the kinetics of ionics fluxes flowing through the ions channels in comparison with the diffusion of ions in between the inter-discs spacings and between the IS and OS mediums. On the numerical aspects, more work needs to be done to optimize the processing algorithms and to decrease the computational requirements. For example, a significant reductions in processing time and memory requirements can be made by including the far-field transform as part of the simulation processing rather than a separate post-processing step. Finally, there is a promising opportunity for research work on the compensation of the effects of numerical dispersion on far-fields results.

Bibliography

[1] J. Beuthany, O. Minety, J. Helfmannz, M. Herrigz, and G. Mller. The spatial variation of the refractive index in biological cells. *J. Phys. Med. Biol.*, 41(3):369–382, March 1996.

[2] K. Bizheva, R. Pflug, B. Hermann, B. Povazay, H. Sattmann, P. Qiu, E. Anger, H. Reitsamer, S. Popov, J. R. Taylor, A. Unterhuber, P. Ahnelt, and W. Drexler. Optophysiology: Depth-resolved probing of retinal physiology with functional ultrahigh-resolution optical coherence tomography. *Proc. Natl. Acad. Sci. U. S. A.*, 103(13):5066–5071, March 2006.

[3] V. J. Srinivasan, M. Wojtkowski, J. G. Fujimoto, and J. S. Duker. In vivo measurement of retinal physiology with high-speed ultrahigh-resolution optical coherence tomography. *J. Opt. Lett.*, 31(15):2308–2310, July 2006.

[4] Xin-Cheng Yao, Angela Yamauchi, Beth Perry, and John S. George. Rapid optical coherence tomography and recording functional scattering changes from activated frog retina. *J. Appl. Opt.*, 44(11):2019–2023, April 2005.

[5] R. A. Stepnoski, A. LaPorta, F. Raccuia-Behling, G. E. Blonder, R. E. Slusher, and D. Kleinfel. Noninvasive detection of changes in membrane potential in cultured neu-

rons by light scattering. *Proc. Natl. Acad. Sci. U. S. A.*, 88(21):9382–9386, November 1991.

[6] K. P. Hofmann, R. Uhl, W. Hoffmann, and W. Kreutz. Measurements of fast light-induced light-scattering and -absorption changes in outer segments of vertebrate light sensitive rod cells. *J. Biophys. Struct. Mech.*, 2(1):61–77, March 1976.

[7] Andrew Dunn, Colin Smithpeter, Ashley J. Welch, and Rebecca Richards-Kortum. Finite-difference time-domain simulation of light scattering from single cells. *J. Biomed. Opt.*, 2(3):262–266, July 1997.

[8] Andrew Kenneth Dunn. *Light Scattering Properties of Cells*. Phd, Univ. Texas at Austin, August 1997.

[9] Rebekah Drezek, Martial Guillaud, Thomas Collier, Iouri Boiko, Anais Malpica, Calum Macaulay, Michele Follen, and Rebecca Richards-Kortum. Light scattering from cervical cells throughout neoplastic progression: influence of nuclear morphology, dna content, and chromatin texture. *J. Biomed. Opt.*, 8(1):7–16, January 2003.

[10] Rebekah Drezek, Andrew Dunn, and Rebecca Richards-Kortum. A pulsed finite-difference time-domain (fdtd) method for calculating light scattering from biological cells over broad wavelength ranges. *J. Opt. Express*, 6(7):147–157, March 2000.

[11] Nader Nassif, Barry Cense, B. Hyle Park, Seok H. Yun, Teresa C. Chen, Brett E. Bouma, Guillermo J. Tearney, and Johannes F. de Boer. *In vivo* human retinal imaging by ultrahigh-speed spectral domain optical coherence tomography. *J. Opt. Express*, 29(5):480–482, 2004.

[12] Peter Forbes, Prabakar Puvanathasan, Doug Machow, and Kostadinka Bizheva. Ultrafast, ultrahigh resolution optical coherence tomography at 1060 nm. poster, 2007.

[13] G. S. Hagerman and L. V. Johnson. *The photoreceptor-retinal pigmented epithelium interface*. Principles and Practice of Clinical Electrophysiology of Vision. Mosby Year Book, St. Louis, 1991. pp. 53-68.

[14] F. L. Tobey J. M. Enoch and H. E. Bedell. *Vertebrate Photoreceptor Optics*. Springer Verlag, first edition, 1981.

[15] M. J. Hogan, J. A. Alvarado, and E. J. Weddell. *Histology of the human eye*. Saunders, Philadelphia, 1971.

[16] Q.V. Hoang, R.A. Linsenmeier, C.K. Chung, and C.A. Curcio. Photoreceptor inner segments in monkey and human retina: Mitochondrial density, optics, and regional variation. *J. Vis. Neurosci.*, 19(4):395–407, July 2002.

[17] William M. Hart, editor. *Adler's Physiology of the Eye*. Mosby Year Book, 1992.

[18] Eric R. Kandel, James H. Schwartz, and Thomas M. Jessell. *Principles of Neural Science*. McGraw-Hill Professional, fourth edition, 2000.

[19] E. A.Dratz, G. P. Miljanich, P. P. Nemes, J. E. Gaw, and S. Schwartz. The structure of rhodopsin and its disposition in the rod outer segment disk membrane. *Photochem. Photobiol.*, 29(4):661–670, Apr 1979.

[20] Richard W. Young. The renewal of rod and cone outer segments in the rhesus monkey. *J. Cell. Biol.*, 49(2):303–318, 1971.

[21] J. G. Hollyfield and M. E. Rayborn. Photoreceptor outer segment development: light and dark regulate the rate of membrane addition and loss. *Invest. Ophthalmol. & Visual Sci*, 18(2):117–132, Feb 1979.

[22] Richard W. Young and Dean Bok. Participation of the retinal pigment epithelium in the rod outer segment renewal process. *J. Cell. Biol.*, 42(2):392–403, Aug 1969.

[23] Richard. W. Young. The organization of vertebrate photoreceptor cells. *UCLA Forum Med. Sci.*, 8:177–210, 1969.

[24] S. E. Nilsson. Receptor cell outer segment development and ultrastructure of the disk membranes in the retina of the tadpole (rana pipiens). *J. Ultrastruct. Res.*, 11:581–602, Dec 1964.

[25] E. De Robertis and A. Lasansky. Ultrastructure and chemical organization of the photoreceptors. *Arch. Oftalmol. B. Aires.*, 40(6):111–123, Jun 1965.

[26] F. S. Sjostrand and M. Kreman. Molecular structure of outer segment disks in photoreceptor cells. *J. Ultrastruct. Res.*, 65(3):195–226, Dec 1978.

[27] Bessie Borwein, David Borwein, John Medeiros, and J. William McGowan. The ultrastructure of monkey foveal photoreceptors, with special reference to the structure, shape, size, and spacing of the foveal cones. *Am. J. Anat.*, 159(2):125–146, October 1980.

[28] M. A. Ali. Les reponses retinomotrices: Caracteres et mecanismes. *Vision Res.*, 11(11):1225–1288, Nov 1971.

[29] H. Asai, T. Chiba, S. Kimura, and M. Takagi. A light-induced conformational change in rod photoreceptor disc membrane. *Exp. Eye Res.*, 21(3):259–267, Sep 1975.

[30] David G. McConnell, Charles N. Rafferty, and Richard A. Dilley. The light-induced proton uptake in bovine retinal outer segment fragments. *J. Biol. Chem.*, 243(22):5820–5826, Nov 1968.

[31] R. Uhl, K. P. Hofmann, and W. Kreutz. Measurement of fast light-induced disc shrinkage within bovine rod outer segments by means of a light-scattering transient. *Biochim. Biophys. Acta.*, 469(2):113–122, Sep 1977.

[32] Jay M. Enoch. The use of tetrazolium to distinguish between retinal receptors exposed and not exposed to light. *Invest. Ophthalmol. & Visual Sci*, 2:16–23, 1963.

[33] S. Johnsen and E. A. Widder. The physical basis of transperancy in biological tissue: ultrastructure and the minimization of light scattering. *J. Theor. Biol.*, 199(2):181–198, July 1999.

[34] Roland Thar and Michael Khl. Propagation of electromagnetic radiation in mitochondria? *J. Theor. Biol.*, 230(2):261–270, July 2004.

[35] N.W. Roberts and H.F. Gleeson. The absorption of polarized light by vertebrate photoreceptors. *Vision Res.*, 44(23):2643–2652, October 2004.

[36] P. A. Liebman, W. S. Jagger, M. W. Kaplan, and F. G. Bargoot. Membrane structure changes in rod outer segments associated with rhodopsin bleaching. *Nature*, 251:31–36, September 1974.

[37] Allan W. Snyder and Colin Pask. The stiles-crawford effect–explanation and consequences. *Vision Res.*, 13(6):1115–1137, June 1973.

[38] Richard L. Sidman. The structure and concentration of solids in photoreceptor cells studied by refractometry and interference microscopy. *J. Biophys. Biochem. Cytol.*, 3(1):15–30, Jan 1957.

[39] Ted Mar. Measurement of mitochondrial volume independent of refractive index by light scattering. *J. Biochem. Bioph. Methods*, 4(3-4):177–184, March 1981.

[40] M. Iwasaki and H. Inomata. Lipofuscin granules in human photoreceptor cells. *Invest. Ophthalmol. & Visual Sci*, 29(5):671–679, May 1988.

[41] Brian Vohnsen, Ignacio Iglesias, and Pablo Artal. Guided light and diffraction model of human-eye photoreceptors. *J. Opt. Soc. Am. A, Opt. image sci. vis.*, 22(11):2318–2328, November 2005.

[42] Kane Yee. Numerical solution of inital boundary value problems involving maxwell's equations in isotropic media. *IEEE Trans. Antennas Propagat.*, 14(3):302–307, May 1966.

[43] Allen Taflove. *Computational Electrodynamics: The Finite-Difference Time-Domain Method*. Artech House, first edition, 1995.

[44] Jay M. Enoch and G. M. Hope. An analysis of retinal receptor orientation: Iii results of initial psychophysical tests. *Invest. Ophthalmol. & Visual Sci*, 11(9):765–782, Sep 1972.

[45] Jay M. Enoch and G. M. Hope. Directional sensitivity of the foveal and parafoveal retina. *Invest. Ophthalmol. & Visual Sci*, 12(7):497–503, Jul 1973.

[46] C. P. O'Connell. The structure of the eye of sardinops caerulea, engraulis mordax, and four other pelagic marine teleosts. *J. Morphol*, 113(2):287–329, Sep 1963.

[47] Adolph I. Cohen. Electron microscope observations on form changes in photoreceptor outer segments and their saccules in response to osmotic stress. *J. Cell. Biol.*, 48(3):547–565, March 1971.

[48] Frank D. Hastings, John B. Schneider, and Shira L. Broschatc. A finite-difference time-domain solution to scattering from a rough pressure-release surface. *J. Acoust. Soc. Am.*, 102(6):3394–3400, December 1997.